Differential Bcd activation of two *hunchback* promoters emerges from unified kinetics of enhancer-promoter interaction

Jingyao Wang[1,2], Shihe Zhang[2,3,*], Hongfang Lu[1,2], and Heng Xu[2,3,4,*]

[1]School of Life Sciences and Biotechnology, Shanghai Jiao Tong University, Shanghai 200240, China

[2]Institute of Natural Sciences, Shanghai Jiao Tong University, Shanghai 200240, China

[3]School of Physics and Astronomy, Shanghai Jiao Tong University, Shanghai 200240, China

[4]Lead Contact

*Correspondence: hsx_sjtu@sjtu.edu.cn (S.Z.), Heng_Xu@sjtu.edu.cn (H.X.)

SUMMARY

Many eukaryotic genes contain alternative promoters with distinct expression patterns. How these promoters are differentially regulated remains elusive. Here, we apply single-molecule imaging to quantify the transcriptional regulation of two alternative promoters (P1 and P2) of the Bicoid (Bcd) target gene *hunchback* in syncytial blastoderm *Drosophila* embryos. Contrary to the previous notion that Bcd only activates P2, we find that Bcd activates both promoters via the same two enhancers. P1 activation is less frequent and requires binding of more Bcd molecules than P2 activation. Using a theoretical model to relate promoter activity to enhancer states, we show that the two promoters follow common transcription kinetics driven by sequential Bcd binding at the two enhancers. Bcd binding at either enhancer primarily activates P2, while P1 activation relies more on Bcd binding at both enhancers. These results provide a quantitative framework for understanding the dynamics of complex eukaryotic gene regulation.

KEYWORDS: *Drosophila* embryo, *hunchback*, alternative promoters, Bicoid, transcriptional regulation, transcription factor binding, synergistic enhancer action

INTRODUCTION

Promoters initiate gene transcription by interacting with specific *cis*-regulatory sequences (enhancers) (Haberle and Stark, 2018; Levine, 2010; Vernimmen and Bickmore, 2015). In eukaryotic genomes, many genes contain alternative promoters (Carninci et al., 2006; Rach et al., 2009), which can produce functionally distinct transcript isoforms under the regulation of multiple enhancers (Davuluri et al., 2008; Kvon et al., 2014; Landry et al., 2003; Ushijima et al., 2017). The differential expression of these isoforms is critical to important biological processes (Lu et al., 2020; Pozner et al., 2007). Misregulation of these isoforms can lead to diseases, including cancer (Davuluri et al., 2008; de Klerk and t Hoen, 2015; Kvon et al., 2021; Sendoel et al., 2017). Thus, eukaryotic gene regulation needs to be understood at the level of individual alternative promoters and enhancers.

Enhancer activation of a single promoter involves a series of molecular events, including transcription factor (TF) binding (Benabdallah et al., 2019; Petrascheck et al., 2005), local chromatin opening (Hnisz et al., 2016; Ling et al., 2019; Phillips-Cremins and Corces, 2013), and physical proximity between the two elements (Benabdallah et al., 2019; Chen et al., 2018; Levine, 2010; Vernimmen and Bickmore, 2015). Typically, TF binding determines the spatial expression pattern (Levine, 2010; Spitz and Furlong, 2012), whereas other events set the expression amplitude (Benabdallah et al., 2019; Foo et al., 2014; Hnisz et al., 2016; Li et al., 2014; Sun et al., 2015). When multiple promoters and enhancers are present, interactions between these elements often result in complex and varied promoter behaviors (Furlong and Levine, 2018). For example, multiple enhancers may contact each other and synergistically drive a promoter (Ghavi-Helm et al., 2014; Oudelaar et al., 2018). Alternatively, different enhancers may be mutually exclusive and compete for promoter activation (Bothma et al., 2015; Scholes et al., 2019). In these cases, enhancers combine their regulatory effects differently, ranging from superadditive to subadditive or even repressive summation (Kvon et al., 2021). Similarly, a single enhancer may activate multiple promoters simultaneously (Fukaya et al., 2016; Lim et al., 2018) or one at a time (Su et

al., 1991). So far, although specific mechanisms were proposed for some of these phenomena, it is unclear whether universal mechanisms exist for the complex interactions between multiple enhancers and promoters.

An ideal model to investigate alternative promoter regulation is the *Drosophila* gap gene *hunchback* (*hb*), which contains two alternative promoters (P1 and P2, Figure 1A) (Driever and Nusslein-Volhard, 1989; Ling et al., 2019; Perry et al., 2012; Schroder et al., 1988). In early embryogenesis (syncytial blastoderm stage, nuclear division cycles (nc) 10–13), *hb* is expressed in a bursty manner (Garcia et al., 2013; Little et al., 2013; Lucas et al., 2013; Xu et al., 2015) throughout the anterior half of the embryo in response to the concentration gradient of the maternal TF Bicoid (Bcd) (Driever and Nusslein-Volhard, 1989; Driever et al., 1989; Struhl et al., 1989). This expression is believed to be purely from the P2 promoter mediated by two enhancers: a proximal enhancer located next to P2 (Driever and Nusslein-Volhard, 1989; Struhl et al., 1989) and a distal "shadow" enhancer located 4.5 kb upstream (Perry et al., 2011). Cooperative Bcd binding at either enhancer can activate P2 (Ling et al., 2019; Perry et al., 2011). Competitive action of these partially redundant enhancers helps suppress expression noise and ensure a robust expression pattern (Bothma et al., 2015; Kvon et al., 2021; Perry et al., 2011; Perry et al., 2012).

Unlike P2, the P1 promoter is believed to be inactive during early development (Margolis et al., 1995; Wu et al., 2001), due to its lack of Zelda binding sites and TATA box necessary for local chromatin opening (Blythe and Wieschaus, 2016; Ling et al., 2019). Instead, the promoter is activated in late nc14 by a Bcd-independent stripe enhancer (Margolis et al., 1995; Perry et al., 2012). However, previous measurements of endogenous P1 activity relied on traditional *in situ* hybridization methods, which have limited sensitivity to detect weak mRNA signals. In fact, *hb*-reporter experiments showed that P1 could respond to Bcd when placed adjacent to the proximal or distal enhancers (Ling et al., 2019). Without precise quantification of endogenous P1 activity,

the understanding of early *hb* regulation is incomplete. It is unclear how P1 interacts with different *hb* enhancers and whether the mechanisms of P1 and P2 regulation are intrinsically related.

Here, we used single-molecule fluorescence *in situ* hybridization (smFISH) (Femino et al., 1998; Little et al., 2013; Raj et al., 2008; Xu et al., 2015) to quantify the expression of individual P1 and P2 promoters for each endogenous *hb* gene locus in nc11–13 embryos. Contrary to the previous notion, we found that P1 contributes a modest yet non-negligible fraction of bursty *hb* transcription in early development. Using different TF dosages and enhancer deletion, we showed that Bcd activates both promoters via the proximal and distal enhancers. Compared with P2, P1 activation requires cooperative binding of more Bcd molecules and a synergistic (as opposed to competitive) action of the two enhancers. Analyzing the statistics of nascent mRNA signals from individual promoter loci revealed that both promoters follow a unified scheme of three-state transcription kinetics. Cooperative Bcd binding at either enhancer can drive a promoter to a weak active state, while additional Bcd binding at the second enhancer can turn the promoter to full-power transcription. The two promoters differ in their responses to different Bcd binding configurations. P2 transcription is primarily driven by Bcd binding at a single enhancer, while P1 transcription relies more on Bcd binding at both enhancers. In concert, these results provide a simple and quantitative mechanism for the differential regulation of alternative promoters. Our quantitative approach may be generalized as a framework for deciphering complex eukaryotic gene regulation involving multiple promoters and enhancers.

RESULTS

hb P1 and P2 promoters are both active in early embryogenesis.

Previous studies reported that each *hb* promoter produces a unique transcript isoform (P1: *hb*-RB, P2: *hb*-RA) (Driever and Nusslein-Volhard, 1989; Tautz et al., 1987). To quantify the endogenous P1 and P2 activities in early embryos, we applied smFISH with four sets of oligonucleotide probes designed for different regions of *hb* mRNAs. Specifically, two P1-specific probe sets targeted the 5' untranslated region (UTR) and intron region of *hb*-RB. A P2-specific probe set targeted the 3'UTR of *hb*-RA. Finally, a probe set targeted the coding sequence (CDS) region shared by *hb*-RA and *hb*-RB. (Figure 1A; Table S1).

Confocal imaging and automated image analysis identified actively transcribing *hb* loci as bright FISH spots in wild-type (WT) syncytial blastoderm embryos (Figure 1B). We quantified the instantaneous transcriptional activity of every locus in units of individual cytoplasmic mRNAs (Xu et al., 2015) (Figure 1B; STAR Methods). For the CDS signal, we observed two bright FISH spots in most anterior nuclei of nc11–13 embryos (Figure 1C; Figure S1A), consistent with previous literature (Little et al., 2013; Porcher et al., 2010; Zoller et al., 2018). It indicates that at least one of the two *hb* promoters is active in the anterior side of the embryo.

Similar to the CDS signal, promoter-specific FISH signals were also concentrated in the anterior half of nc11–13 embryos (Figure 1C). Specifically, ~50% of the anterior loci (within the range of 0.20–0.40 embryo length (EL)) showed bright P2-3'UTR spots (Figure 1D), consistent with previous reports of active P2 expression in early development (Ling et al., 2019; Schroder et al., 1988). Surprisingly, ~18%–34% of the anterior loci in nc11–13 embryos also contained bright P1-5'UTR and intron spots (Figure 1D). The percentage of P1-active anterior loci increased with the nuclear cycle (Figure 1D), suggesting that P1 becomes increasingly active during development. In total, P1- and P2-specific probe signals were exhibited in ~64%–76% of the anterior loci, lower than that of the CDS signal. This percentage difference may be because the P2-specific probes target the very end of *hb*-RA, which is missing in many incomplete nascent transcripts. Alternatively, some P2 transcripts may terminate at a proximal site without passing the target region of our probes (Bender et al., 1988).

To analyze the instantaneous transcription of P1 and P2, we plotted, for each probe set, the number of nascent mRNAs against the nuclear position for all loci in the embryo (Figures 1B). During nc11–13, the average expression profile for each probe set exhibited a reverse-sigmoidal shape within the range 0.25–0.75 EL (Figures 1E). By fitting the profile to a logistic function, we estimated the maximal transcription level r_{max} and the boundary position x_0 of the anterior expression domain (STAR Methods). As expected, r_{max} of P1-specific signals was much smaller than that of the CDS signal (Figure 1F), indicating that P1 contributes less than P2 to early *hb* expression. r_{max} of the P2-specific signal also remained low (Figure 1F), as the probe set targets the 3'UTR of *hb*-RA. In contrast, active P1 and P2 loci exhibited much more nascent mRNAs (Figure S1B), suggesting that both promoters perform intensive expression once active. The boundary position x_0 of the P1-specific signals was significantly lower than that of the P2-specific and CDS signals (~0.42 EL v.s. ~0.46EL, $p<0.05$, Student's t-test, Figure 1G), indicating that P1 is activated at a more anterior position than P2.

In addition to the mean expression level, the activities of individual promoter loci exhibited substantial variability (Figures 1B). The Fano factors of anterior P1- and P2-specific signals were much larger than one (Figure 1H; STAR Methods), indicating bursty transcription from both promoters (Raj et al., 2006; Sanchez and Golding, 2013). Further analysis showed that such burstiness resulted from the intrinsic stochasticity of *hb* transcription, with the two promoters behaving independently (Figure S1C and S1D; STAR Methods).

P1 contributes a modest yet non-negligible fraction of nascent *hb* transcription.

To quantify the contributions of P1 and P2 to nascent *hb* transcription, we note that the *hb* CDS signal reflects either P1 or P2 transcription. At steady state, the nascent CDS signal from a specific promoter should be, on average, proportional to the signal of promoter-specific probes (STAR Methods). Thus, the observed nascent CDS signal (r_{CDS}) should be a linear combination of the

nascent P1-5'UTR and P2-3'UTR signals (r_{P1} and r_{P2}):

$$r_{CDS} = a_1 r_{P1} + a_2 r_{P2} \quad (1)$$

where a_1 and a_2 are ratio parameters that depend on the mRNA elongation and termination dynamics (STAR Methods)(Zoller et al., 2018). The two terms on the right-hand side of the equation distinguish the contribution of each promoter to the CDS signal.

To examine **Equation (1)**, we compared P1-5'UTR, P2-3'UTR, and CDS signals in the same embryo (Figure 2A). The three signals from P1- and P2-active gene loci satisfied a linear relationship (Figure 2B) with a_1 = 0.53 ± 0.07 and a_2 = 2.74 ± 0.16 (Figure 2C). In a simple transcription model with deterministic elongation and termination processes (Xu et al., 2016; Zoller et al., 2018), the above a_1 and a_2 values indicate a post-elongation residence time (T_R) in terminating a nascent mRNA (Figure 2D; Figure S2A; STAR Methods). The estimated T_R for P1 and P2 was 142 s and 46 s, respectively, consistent with previous estimations of transcription termination (Bentley, 2014; Lenstra et al., 2016; Zoller et al., 2018). These results validate **Equation (1)** and enable the decomposition of the CDS expression profile into different promoter activities (Figure 2E; Figure S2B-S2D; STAR Methods). In the anterior expression domain, the contribution of P1 increased with the nuclear cycle to ~13% (Figure 2F), which was modest yet non-negligible.

In addition to the mean expression level, we investigated the contributions of P1 and P2 to the variability of nascent *hb* transcription quantified by the intrinsic noise of the single-locus data (Waymack et al., 2020):

$$\eta^2 = \frac{\langle (m_1 - m_2)^2 \rangle}{2\langle m_1 \rangle \langle m_2 \rangle} \quad (2)$$

where m_1 and m_2 are the numbers of nascent mRNAs at two homologous loci in the same nucleus,

respectively (STAR Methods). During nc11–13, the intrinsic noise of P1 was 2–5 times higher than that of P2 in the anterior expression domain (Figure 2G). This was mainly due to the low expression level of P1. Since the CDS signal is the sum of P1 and P2 activities, its intrinsic noise is significantly lower than that of P2 by ~5 folds ($p<0.01$, Student's t-test Figure 2G). Considering that P1 and P2 activities were independent (Figures S1D), their contributions to CDS noise could be summed as:

$$\eta^2_{\text{CDS}} = \eta^2_{\text{P1-CDS}} f^2_{\text{P1-CDS}} + \eta^2_{\text{P2-CDS}} f^2_{\text{P2-CDS}} \quad (3)$$

where $\eta^2_{\text{P1-CDS}}$ and $\eta^2_{\text{P2-CDS}}$ denote CDS noises originating from P1 and P2 activities, respectively, while $f_{\text{P1-CDS}}$ and $f_{\text{P2-CDS}}$ indicate the relative contributions of each promoter to the mean CDS signal (STAR Methods). **Equation (3)** revealed that P1 contributed to up to ~20% of the anterior CDS noise during nc11–13 (Figure 2H), which exceeded its contribution to the mean CDS signal.

Activating P1 requires cooperative binding of more Bcd molecules than activating P2.

In early embryogenesis, the exponential gradient of Bcd is the primary driver of anterior *hb* transcription (Driever and Nusslein-Volhard, 1989; Lehmann and Nusslein-Volhard, 1987; Struhl et al., 1989). To examine whether Bcd directly regulates both promoters, we used a transgenic fly line with 1× functional *bcd* gene (Liu and Ma, 2013). With reduced Bcd dosage, the anterior expression domains of P1 and P2 both retreated towards the anterior pole (Figure 3A). Specifically, P1 and P2 expression boundaries in 1× *bcd* embryos significantly shifted to the anterior side by ~0.07 EL ($p<0.01$, Student's t-test, Figure 3B). Thus, Bcd activates both promoters in nc11–13 embryos.

To quantify the regulation of each promoter by Bcd, we combined promoter-specific smFISH of *hb* mRNA with immunofluorescence of Bcd (Figure 1B). We estimated the absolute Bcd concentration in each nucleus using a previously developed image analysis method (Xu et al., 2015) (STAR Methods). For each promoter, we plotted the average transcriptional response of a gene locus (0.25–0.75 EL) to nuclear Bcd concentration in the embryo (Figure 3C), known as the gene regulation function (GRF) (Rosenfeld et al., 2005). Previous studies reported that *hb* GRF fitted well to a Hill function with a Hill coefficient $h \approx 5$–6 (Gregor et al., 2007; Lopes et al., 2012; Xu et al., 2015). A common explanation was that Bcd activates *hb* by cooperatively binding multiple sites in the regulatory sequence (Driever et al., 1989; Estrada et al., 2016; Lopes et al., 2005; Ma et al., 1996). Here, we found that the Hill coefficient of P1-specific GRFs (P1-5'UTR: $h = 7.1 \pm 0.4$, P1-intron: $h = 7.2 \pm 0.3$, mean ± s.e.m.) was significantly higher than that of P2-specific ($h = 4.6 \pm 0.2$) and CDS ($h = 5.3 \pm 0.3$) GRFs during nc11–13 ($p<0.05$, Figure 3D). These results indicate that P1 activation corresponds to higher-order cooperative binding than P2 activation. Moreover, P1-specific signals exhibited a higher concentration threshold C_0 for activation than P2-specific and CDS signals, with their ratios being consistently larger than one (Figure 3E**)**. This agrees with our observation of P1 and P2 expression boundaries (Figure 1G).

To directly quantify Bcd binding corresponding to P1 and P2 activation, we measured local enrichment of the Bcd signal in the vicinity of P1- and P2-active *hb* loci (He et al., 2011; Xu et al., 2015) (Figure 3F; STAR Methods). In the anterior expression domain of nc11–12 embryos, we estimated an average binding of ~6.2 Bcd molecules at P1-active loci, exceeding that of ~4.7 Bcd molecules at P2-active loci (Figure 3F). This result confirmed that P1 activation requires cooperative binding of more Bcd molecules than P2 activation. In nc13, along with the increase in P1 activity (Figure 1D and 1F), the number of bound Bcd molecules at P1-active loci dropped to ~5.4. Examining how Bcd binding at active promoter loci varied with nuclear Bcd concentration (or nuclear position) revealed that both P1- and P2-specific binding curves plateaued at ~4–5 Bcd molecules, while the P1-specific binding curve exhibited an additional plateau with ~8–10 Bcd molecules in nc11–12 (Figure 3G; Figure S3). As suggested previously, these plateaus may

correspond to distinct Bcd binding states at *hb* enhancers (Xu et al., 2015). The additional Bcd binding plateau for P1 implies that P1 activation may involve more Bcd-binding steps than P2 activation. This additional plateau decreased to ~6 Bcd molecules in nc13, implying a change in Bcd binding dynamics.

Two Bcd-dependent enhancers synergistically drive P1 activation.

Two Bcd-dependent enhancers are involved in early *hb* regulation. To distinguish their roles in P1 and P2 activation, we used transgenic fly lines derived from a bacterial artificial chromosome (BAC) containing the *hb* gene and its regulatory sequence (Perry et al., 2011) (Figure 4A; STAR Methods). The transgenes retained the *hb* promoters, introns, and UTRs, whereas the *hb* CDS was replaced with a *yellow* reporter gene. The distal and proximal enhancers of the two transgenes were substituted, respectively, while the regulatory sequence of the third transgene was kept intact as a control.

To measure the promoter activities of the transgene, we labeled transgenic embryos with three sets of smFISH probes targeting P1 intron, *hb* CDS, and *yellow*, respectively (Figure 4B). The P1 signal corresponding to the endogenous *hb* gene was identified and excluded based on its colocalization with the *hb* CDS signal. We compared the anterior P1 and *yellow* (mainly from P2) signals in the control and enhancer-removed transgenes in nc11–13 embryos (Figures 4C; Figures S4A and S4B). The control transgene was active (with a nascent *yellow* signal) in >70% of the anterior loci (Figure 4D), similar to the endogenous *hb* gene. Removal of either enhancer significantly lowered the percentage of the *yellow*-positive anterior loci by >16% ($p<0.05$, Student's t-test) in nc11–12. This finding is consistent with previous reports that both enhancers are required for authentic *hb* expression (Bothma et al., 2015; Ling et al., 2019). In contrast, removing the proximal but not the distal enhancer lowered the percentage of P1-active anterior loci by >26% in nc11–13 embryos (Figure 4C and 4D), suggesting that early P1 activation relies

more on the proximal enhancer.

Comparing the *yellow* expression profiles between the control and enhancer-removed transgenes (Figures 4E; Figure S4C and S4D) revealed a decrease in the maximum anterior expression level r_{max} by ~34.5% in response to proximal or distal enhancer removal (Figure 4F). This agrees with a previous report that P2 subadditively integrates regulatory inputs from different enhancers via enhancer competition (Bothma et al., 2015). In contrast, removing the proximal enhancer decreased the maximum expression level r_{max} of P1 by >50% in nc11–12, while removing the distal enhancer barely changed r_{max} of P1 (Figure 4F). These results confirmed that the early P1 expression amplitude is primarily determined by the proximal enhancer.

Besides affecting the expression amplitude, both enhancers are critical for promoter expression boundaries. Specifically, removing the proximal enhancer shifted the *yellow* expression boundary towards the anterior pole, while removing the distal enhancer caused a posterior shift of the *yellow* profile (Figures 4G). These results agree with the enhancer competition model for P2 activation (Bothma et al., 2015), in which the expression boundary resulting from two enhancers lies between that from individual ones. In contrast, the deletion of either enhancer caused an anterior shift of the P1 expression boundary (Figures 4H), which is inconsistent with the enhancer competition model. It shows that the existence of a second enhancer helps activate P1 at lower Bcd concentration. Thus, the two enhancers may interact synergistically to drive P1 activation.

Promoter-specific transcription kinetics reveal a unified scheme of enhancer-promoter interaction

Nascent mRNA copy number statistics reflect the microscopic mechanisms of gene regulation (Munsky et al., 2012; Zenklusen et al., 2008). Previous studies reported a super-Poissonian

distribution of the nascent mRNA copy number on individual *hb* gene loci (Little et al., 2013; Xu et al., 2015; Zoller et al., 2018). Such distribution can be explained by a minimal model of two-state transcription kinetics (Peccoud and Ycart, 1995; Raj et al., 2006; Senecal et al., 2014; Xu et al., 2016; Zenklusen et al., 2008) with Bcd modulating the frequency of stochastic transition from an inactive to an active transcription state (Xu et al., 2015; Zoller et al., 2018).

To uncover the kinetics of P1 and P2 transcription, we measured, for each embryo, the distributions of P1 and P2 nascent mRNA signals in different Bcd concentration ranges (Figure 5A). Contrary to the prediction from the two-state model (Munsky et al., 2012; Xu et al., 2016), each promoter exhibited a wide distribution with more than one population of active loci characterized by different expression levels (Figure 5A). A natural explanation of this phenomenon is that some of the observed promoter loci may indeed be a pair of closely located sister loci that are indistinguishable under the microscope (Little et al., 2013; Zoller et al., 2018). However, the nascent mRNA signal from optically resolved sister loci pairs also exhibited two active populations, with >38% of P1 and >17% of P2 active sister loci corresponding to the minor population (Figure 5B; STAR Methods). Thus, P1 and P2 transcription must be modeled as a three-state process (Ferraro et al., 2016).

In this model, a promoter randomly switches between an inactive state (state 0) and two active states (states 1 and 2) with Poissonian rates k_{ij} (i, j = 0, 1, 2), whereas new transcripts are only initiated in active states with rates $k_{\mathrm{INI},i}$. Following transcription initiation, each nascent mRNA elongates with constant speed V_{EL}, and resides on the gene for an extra termination period T_{R} before being released (Figure 5A). With a detailed balance between states, we solved the steady-state distribution of nascent mRNAs per promoter locus and compared it with experimental data to infer the kinetic parameters (Figure 5A; STAR Methods). We found that P1 and P2 both followed a sequential activation scheme from state 0 to state 2 (Figure S5A; STAR Methods). Bcd mainly regulated the activation rates, k_{01} and k_{12}, while other kinetic rates remained constant (Figure S5B).

For both promoters, the Bcd dependence of k_{01} and k_{12} satisfied Hill functions (Figure 5C), with the corresponding Hill coefficient h and concentration threshold C_0 identical between the promoters (Figure 5D and 5E). Specifically, the Hill coefficient of k_{01} was ~4.5 (P1: h = 5.2 ± 0.5, P2: h = 4.0 ± 0.5, Figure 5D), close to that of P2-GRF. In contrast, the Hill coefficient of k_{12} was ~10 (P1: h = 10.0 ± 1.0, P2: h = 10.1 ± 1.0, Figure 5D). h of k_{01} and k_{12} each matched a plateau in the Bcd binding curves of *hb* promoters (Figure 3G), suggesting that each promoter activation step may involve a cooperative Bcd binding event. The concentration threshold of k_{01} was ~24 nM (P1: C_0 = 23.5 ± 2.5, P2: C_0 = 23.9 ± 2.6, Figure 5E), which was close to that of P2-GRF. In contrast, the concentration threshold of k_{12} was only ~17 nM (P1: C_0 = 17.1 ± 2.6, P2: C_0 = 17.2 ± 2.4, Figure 5E), suggesting that the second Bcd-binding event is easier to happen than the first one.

In addition to the Bcd dependence, the ratio between the activation and inactivation rates determines the probability of each transcription state. In the anterior expression domain, k_{01}/k_{10} for P1 was smaller than that for P2 by >5 folds (Figure S5C), indicating that P2 is more likely to be activated than P1. In contrast, k_{12}/k_{21} for P1 exceeded that for P2 by >2 folds (Figure S5D), indicating that active P1 is more inclined to reach state 2 than active P2. For each active state (i = 1, 2), the transcription initiation rate $k_{INI,i}$ for P1 were lower than that for P2 (Figure 5F). However, since $k_{INI,2}$ of P1 was close to $k_{INI,1}$ of P2, mRNA production from active P1 loci was comparable to that of active P2 loci (Figure S1B). Specifically, State 2 contributed much more to P1 transcription than to P2 transcription (57.7% vs. 25.7%, Figure 5G). This explains the difference (in h and C_0) between the P1- and P2-GRFs. I.e., the differential regulation of P1 and P2 results from their preference for different active states.

To relate transcription kinetics with enhancer activities, we applied theoretical analysis to enhancer deletion experiments. For early P1 transcription (nc11-12), the removal of either enhancer yielded a uniform decrease of k_{01} by ~30% in the anterior expression domain (Figure 5H; Figure S5E). Deleting the proximal enhancer also caused a modest anterior shift of the k_{01}

boundary (Figure 5H). These results suggest that either enhancer can drive promoter activation to state 1. In contrast, deleting either enhancer caused a dramatic anterior shift of the k_{12} boundary (Figure 5H; Figure S5F). This indicates that state 2 is primarily driven by the synergistic action of both enhancers. When the Bcd concentration is sufficiently high, state 2 may also be driven by a single enhancer, possibly due to extra Bcd binding at weak binding sites. These mechanisms explain the difference between P1 and P2 in the expression boundary shift upon enhancer removal (Figure 4G and 4H).

Altogether, we propose that the two *hb* promoters follow a common kinetic scheme of Bcd-dependent activation (Figure 5I; STAR Methods). Cooperative Bcd binding at either enhancer can drive a promoter to a basal active state, while full-power transcription requires additional Bcd binding at the second enhancer. The two promoters differ in their responses to different Bcd binding configurations. P2 is primarily activated by Bcd binding at a single enhancer, which results in competitive action of the two enhancers. In contrast, P1 activation relies more on Bcd binding at both enhancers, which leads to synergistic enhancer action. The predicted joint distribution of P1- and P2-specific nascent mRNAs agreed well with experimental results (Figure 5J; STAR Methods).

DISCUSSION

Traditional FISH and lacZ reporter experiments reported that Bcd-dependent *hb* transcription in early embryogenesis only involves the P2 promoter (Driever et al., 1989; Margolis et al., 1995; Struhl et al., 1989; Wu et al., 2001), while P1 is Bcd-insensitive and remains silent until late nc14 (Ling et al., 2019; Margolis et al., 1995; Schroder et al., 1988). Here, using smFISH method with single-molecule sensitivity, we showed that Bcd activated both promoters in the anterior domain

of nc11–13 embryos. P1 contributes up to ~13% of nascent *hb* signal and up to ~20% of nascent *hb* noise. These fractions are modest compared to those of P2, yet significant enough to affect the shape and fluctuation of the *hb* expression pattern. Thus, the Bcd-dependent P1 expression is not negligible.

According to previous studies, the difference in P1 and P2 expression levels is due to specific motif codes in promoter sequences. P2 contains Zelda binding sites and a strong TATA box to facilitate chromatin opening and promoter activation (Foo et al., 2014; Ling et al., 2019; Schulz et al., 2015). In contrast, the lack of Zelda binding sites and TATA box in the P1 promoter significantly impedes local chromatin opening and promoter activation (Blythe and Wieschaus, 2016; Nien et al., 2011; Sun et al., 2015). However, our results suggest that the lack of these motif codes may be insufficient to completely block early P1 activity. In fact, the local chromatin state of a gene has been reported to be highly dynamic and can randomly switch between “open” and “close” to allow transient gene expression (Bintu et al., 2016; Swinstead et al., 2016; Voss and Hager, 2014). This effect has been proposed as a mechanism for transcriptional bursting (Bintu et al., 2016; Eck et al., 2020; Lammers et al., 2020), consistent with our observation of bursty P1 transcription. Moreover, our observation that the percentage of active P1 loci increased with the nuclear cycle suggests a gradual increase in chromatin opening frequency during development. The stronger P1 activity in late nc14 may be a continuation of this trend.

In addition to the expression amplitude, the Bcd dependence of P1 and P2 showed quantitative differences. P1 activation requires a higher Bcd concentration and binding of more Bcd molecules than P2 activation. One possible mechanism for this difference is that the two promoters are driven by different enhancers. However, we showed that early P1 and P2 activation relied on the same pair of enhancers (Perry et al., 2011). Another possibility is that the two promoters distinguish their behaviors by interacting with each other (e.g., mutual repression (Li et al., 2018)). However, we found little correlation between P1 and P2 activities. This is consistent with a previous promoter-deletion experiment (Ling et al., 2019) and indicates no interaction

between the two promoters. Thus, the difference in Bcd dependence originates from complex enhancer-promoter interactions.

One form of complex enhancer-promoter interaction is the competitive action of the proximal and shadow enhancers for *hb* P2 activation (Bothma et al., 2015). Here, each enhancer corresponds to a unique Bcd-dependent regulatory effect, and the two enhancers compete for promoter activation (Kvon et al., 2021). The resulting P2 expression is a sub-additive integration of individual enhancers' regulatory effect. Such a mechanism can lead to a different Bcd-dependent relationship if the enhancers' relative weights in the integration change. However, the P1 expression boundary always shifts anteriorly in response to the deletion of either enhancer, suggesting a synergistic, as opposed to competitive, action of the two enhancers for P1 activation. This result also revealed that the Bcd dependence of P1 and P2 differed even in the case of a single enhancer, indicating that the TF dependence of an enhancer's regulatory effect may be promoter-specific.

To understand the mechanism of promoter-specific interactions with enhancers, we analyzed the transcription kinetics of individual promoters. Unlike the previous model of two-state *hb* transcription (Little et al., 2013; Xu et al., 2015; Zoller et al., 2018), we found that both P1 and P2 activities need to be described by three-state kinetics with sequential activation steps. Multi-step transcriptional activation was previously proposed to model enhancer-, promoter-, or chromatin-related intermediate states during activation (Berry et al., 2017; Bintu et al., 2016; Choubey et al., 2015; Eck et al., 2020; Neuert et al., 2013; Rieckh and Tkacik, 2014; Voss and Hager, 2014). However, these intermediate states are rarely experimentally detectable. In the case of *hb*, previous measurements mixed signals from P1 and P2, whose difference easily overwhelmed the subtle signatures of different transcription states. Here, the identification of multiple active states was possible owing to promoter-specific demixing of the *hb* nascent mRNA signal. Thus, it is important to distinguish alternative promoters in the study of complex gene regulation.

Our model revealed that Bcd regulates both activation steps (k_{01} and k_{12}) through cooperative binding. This suggests that the two active states of a promoter may correspond to different Bcd binding states at *hb*. Previous literature has shown evidence of multiple Bcd binding states at *hb* (Xu et al., 2015). However, only one binding state (with ~4–5 Bcd molecules) was reported to coincide with gene activation (Xu et al., 2015). The biological functions of the other binding states were unclear. Here, we showed that the binding of ~4–5 Bcd molecules happened at a single enhancer (either proximal or distal). Enhancers at this binding state can competitively drive promoter activation, consistent with a previous study of *hb* P2 activation (Bothma et al., 2015). In contrast, the binding of ~8–10 Bcd molecules involved both enhancers, leading to synergistic activation of a promoter. Such a mechanism was proposed for some eukaryotic genes (Bothma et al., 2015; Choi et al., 2021) but has never been reported for *hb*.

P1 and P2 differ in their preference for different Bcd binding states. Specifically, the P1 response to the lower Bcd binding state is much less than that of P2. A possible reason is that P1 lacks specific motif codes for chromatin opening (Ling et al., 2019). Thus, its activation may require TF binding at enhancers to help open the local chromatin configuration (Eck et al., 2020; Lammers et al., 2020). Binding of more Bcd molecules at both enhancers may be more effective for chromatin opening. However, since P1 locates between the two enhancers, binding of Bcd (and other regulatory factors) at the proximal enhancer may physically block P1 transcription. It is unclear how P1 coordinates its activation and transcription. One possibility is that TF binding at enhancers is only transiently needed to form the preinitiation complex. Future experiments using high-resolution live imaging techniques would be likely to solve this puzzle (Chen et al., 2018; Li et al., 2020; Li et al., 2019).

Altogether, these results showed that a single kinetic scheme could create apparently different types of enhancer-promoter interactions. Such a unified scheme may be shared by alternative promoter regulation in many eukaryotic systems and may be crucial for phenotypic complexity in higher eukaryotes (Landry et al., 2003). Moreover, our combined experimental and theoretical

approach directly relates TF binding at individual enhancers with the stochastic activity of each promoter. A generalization of this approach (e.g., by including more regulatory factors) will help understand complex eukaryotic gene regulation in different organisms and enable the precise design of synthetic gene circuits (Doshi et al., 2020).

AUTHOR CONTRIBUTIONS

Conceptualization, J.W. and H.X.; Methodology, J.W., H.L., S.Z., and H.X.; Software, S.Z. and H.X.; Formal Analysis, J.W. and S.Z.; Investigation, J.W., S.Z., and H.X.; Writing – Original Draft, J.W. and H.X.; Funding Acquisition, H.X.; Resources, H.X.; Supervision, H.X.

ACKNOWLEDGMENTS

We thank Jun Ma, Michael Perry, and Alistair Boettiger for the generous gift of fly lines. We thank Ido Golding, Anna Sokac, and Jun Ma for insightful discussion and valuable comments on the manuscript. This work was supported by the National Key R&D Program of China (grant no. 2018YFC0310803), the National Science Foundation of China (grant no. 11774225, 41921006), the National Science Foundation of Shanghai (grant no. 18ZR1419800), and the Burroughs Wellcome Fund Career Award at the Scientific Interface (grant no. 1013907). We gratefully acknowledge the imaging and computing resources provided by the Instrumental Analysis Center and the Student Innovation Center at Shanghai Jiao Tong University.

DECLARATION OF INTERESTS

The authors declare no competing interests.

MAIN FIGURE TITLES AND LEGENDS

Figure 1. Absolute quantification of *hb* transcription reveals P1 and P2 activities in early embryogenesis.

(A) Schematic of the endogenous *hb* locus with two Bcd-dependent enhancers (green: distal enhancer, brown: proximal enhancer) and two promoters (P1 and P2). Each promoter drives the expression of a specific transcript isoform. Four smFISH probe sets were used to label different regions of *hb* mRNAs.

(B) Confocal images of two wild-type *Drosophila* embryos, each labeled for two regions of *hb* mRNAs, Bcd protein, and DNA at nc12. Scale bars, 50 μm. Insets, magnified views of anterior nuclei. Scale bars, 5 μm. The number of nascent mRNAs at individual *hb* loci was plotted against the anterior-posterior (AP) position for different probe signals.

(C) Percentage of active *hb* loci as a function of the AP position for different probe signals during nc11–13. Marked region, 0.2–0.4 EL. Shadings indicate s.e.m.

(D) Average percentage of active *hb* loci in the position range of 0.2–0.4 EL for different probe signals during nc11–13. Error bars represent s.e.m.

(E) The number of nascent mRNAs at individual *hb* loci as a function of the AP position for different probe signals during nc11–13. Marked region, 0.25–0.75 EL. Shadings indicate s.e.m.

(F–G) The maximal transcription level (F) and the boundary position (G) of the anterior expression domain for different probe signals during nc11–13. Error bars represent s.e.m.

(H) The Fano factor for the number of nascent mRNAs at individual *hb* gene loci in the position range of 0.2–0.4 EL for different probe signals during nc11–13.

(C–H) Data averaged from ≥5 embryos for each nuclear cycle. P-values were from Student's t-test: *, p<0.05; **, p<0.01.

Figure 2. P1 contributes a modest yet non-negligible fraction of early *hb* transcription.

(A) Confocal image of a wild-type *Drosophila* embryo colabeled for P1-5'UTR, P2-3'UTR, CDS of *hb* mRNA, and DNA at nc13. Scale bar, 50 μm. Inset, magnified view of anterior nuclei. Scale bar, 5 μm.

(B) The numbers of nascent mRNAs for P1-5'UTR, P2-3'UTR, and CDS signals at individual active *hb* gene loci were plotted against each other and fitted to a linear function. Data from a single nc12 embryo.

(C) Parameters of the linear fit between P1-5'UTR, P2-3'UTR, and CDS signals during nc11–13. Data averaged from two embryos for nuclear cycle 11 and seven embryos each for nuclear cycles 12 and 13. Error bars represent s.e.m.

(D) Schematic of P1 and P2 transcription. Nascent mRNAs were elongated on the gene with a constant speed and stayed on the transcription site for an extra period before being released. The P1-specific intron was spliced during or after transcription.

(E) The contributions of P1 and P2 transcription to the nascent CDS signal at individual *hb* loci as a function of the AP position during nc11–13. Marked region, 0.2–0.4 EL.

(F) Average P1 and P2 contributions to the nascent CDS signal at individual *hb* loci in the position range of 0.2–0.4 EL during nc11–13.

(G) The intrinsic noise for P1-5'UTR, P2-3'UTR, and CDS signals at individual *hb* gene loci in the position range of 0.2–0.4 EL during nc11–13. Error bars represent s.e.m. P-values were from Student's t-test: *, p<0.05; **, p<0.01.

(H) The contributions of P1 and P2 to the intrinsic noise of the nascent CDS signal at individual *hb* gene loci in the position range of 0.2–0.4 EL during nc11–13.

(E–H) Data averaged from ≥5 embryos for each nuclear cycle.

Figure 3. Bcd activates P1 and P2 through different regulatory relations.

(A) The average number of nascent mRNAs at individual *hb* loci for P1-5'UTR and P2-3'UTR signals as a function of the AP position in a 1× *bcd* (solid line) embryo was compared with that in the wild-type (dashed line, data averaged from five embryos). Shadings indicate s.e.m.

(B) The boundary position of the anterior expression domain for P1-5'UTR and P2-3'UTR signals in wild-type and 1× *bcd* embryos during nc11–13. Data averaged from ≥5 wild-type embryos and

four 1× *bcd* embryos for each nuclear cycle. Error bars represent s.e.m. P-values were from Student's t-test: *, p<0.05; **, p<0.01.

(C) The number of nascent mRNAs at individual *hb* loci for P1-5'UTR (upper) and P2-3'UTR (lower) signals was plotted against nuclear Bcd concentration (single wild-type embryo, >1200 nuclei, 0.25–0.75 EL). The single-locus data were binned along the Bcd axis (mean ± s.e.m.) and fitted to Hill functions.

(D) Hill coefficient of the gene regulation function for different probe signals during nc11–13. Error bars represent s.e.m. P-values were from Student's t-test: *, p<0.05; **, p<0.01.

(E) The ratios of the concentration threshold between P1-intron and CDS signals, and between P1-5'UTR and P2-3'UTR signals, during nc11–13. Error bars represent s.e.m.

(F) The average number of Bcd molecules bound at P1- and P2-active *hb* loci in the anterior expression domain (0.2–0.35 EL) during nc11–13. Error bars represent s.e.m. Inset: an anterior nucleus labeled for P1-5'UTR and P2-3'UTR of *hb* mRNAs and Bcd protein. The enriched Bcd signal in the vicinity of the promoter (yellow and purple circles) was measured. Scale bar, 2 μm.

(G) Bcd binding at P1- and P2-active *hb* loci as a function of nuclear Bcd concentration at nc12. The binned data were fitted to multi-Hill functions. Dashed lines highlight discrete binding plateaus for each promoter. Error bars represent s.e.m.

(D–G) Data averaged from ≥5 embryos for each nuclear cycle.

Figure 4. Two enhancers combine differently to drive P1 and P2 activation.

(A) Schematic of *hb* reporter constructs with enhancer replacements. A construct without enhancer deletion was used as a control. Two smFISH probe sets were used to label different regions of reporter mRNAs: blue, P1-intron probes; red, *yellow* probes.

(B) Confocal image of a distal-enhancer-removed embryo labeled for P1-intron, *yellow*, and *hb* CDS at nc12. Scale bar, 50 μm. Inset, magnified view of a single anterior nucleus. Scale bar, 2 μm.

(C) Percentage of active reporter gene loci as a function of the AP position for P1-intron and *yellow* signals in nc12 embryos of different constructs. Shadings indicate s.e.m.

(D) The average percentage of active reporter gene loci in the position range of 0.2–0.4 EL for P1-intron and *yellow* signals in different constructs during nc11–13. Error bars represent s.e.m.

(E) The number of nascent mRNAs at individual reporter gene loci as a function of the AP position for P1-intron and *yellow* signals in nc12 embryos of different constructs. Shadings indicate s.e.m.

(F) The maximal transcription level of the anterior expression domain for P1-intron and *yellow* signals in different constructs during nc11–13. Error bars represent s.e.m.

(G–H) The boundary shift of the anterior expression for *yellow* (G) and P1-intron (H) signals upon removing one enhancer. Error bars represent s.e.m. Right: schematic of boundary shift.

(C–H) Data compared between the distal- or proximal-enhancer-removed constructs and their controls. Data averaged from ≥4 embryos for each reporter construct and each nuclear cycle. P-values were from Student's t-test: *, $p<0.05$; **, $p<0.01$.

Figure 5. Three-state promoter kinetics reveal a unified scheme of P1 and P2 regulation.

(A) Histograms of nascent mRNA at individual *hb* gene loci for P1-5'UTR (upper) and P2-3'UTR (lower) signals in different position ranges (single embryo, the center of each position range is indicated above the histogram). Each histogram was fitted to a three-state transcription model (right).

(B) Histograms of *hb* nascent mRNA at active sister loci for P1-5'UTR (upper) and P2-3'UTR (lower) signals in the position range of 0.2–0.4 EL. Each histogram was fitted to two Poisson distributions. Data pooled from seven embryos at nc13. Insets, images of a single anterior nucleus with active sister loci pairs.

(C) Promoter activation rates for P1 and P2 estimated from five embryos at nc12 were plotted against nuclear Bcd concentration and fitted to Hill functions.

(D–E) The Hill coefficients (D) and concentration thresholds (E) of promoter activation rates for P1 and P2 during nc11–13. Error bars represent s.e.m.

(F) The transcription initiation rates of the two active states for P1 and P2 during nc11–13. Error bars represent s.e.m.

(G) The contributions of states 1 and 2 to P1 and P2 transcription in the position range of 0.2–0.4 EL during nc11–13. Error bars represent s.e.m.

(H) P1 activation rates as functions of the AP position for different constructs at nc12 (≥4 embryos for each reporter construct). Data were normalized and compared between the distal- or proximal-enhancer-removed constructs and the control.

(I) Schematic of P1 and P2 regulation by cooperative Bcd binding at the proximal and distal enhancers.

(J) The joint distribution of nascent P1-5'UTR and P2-3'UTR signals at individual *hb* gene loci in the position range of 0.2–0.4 EL compared with model prediction. Data pooled from 17 embryos during nc11–13. White circles, individual loci. Color code, probability estimated from a unified model of P1 and P2 transcription.

(D–G) Data averaged from ≥5 embryos for each nuclear cycle.

STAR★METHODS

RESOURCE AVAILABILITY

Lead contact

Further information and requests for resources and reagents should be directed to and will be fulfilled by the Lead Contact, Heng Xu (Heng_Xu@sjtu.edu.cn).

Materials availability

All unique/stable reagents and fly strains generated in this study are available from the Lead Contact with a completed Materials Transfer Agreement.

Data and code availability

The raw image data reported in this paper are available at http://gofile.me/4yuzx/wKna2V9pK. Custom scripts for data analysis and mathematical modeling were written in MATLAB 2018a (MathWorks) and are available at https://github.com/Dr-xu-lab/Quantify-the-transcriptional-regulation.

EXPERIMENTAL MODEL AND SUBJECT DETAILS

Fly strains

Oregon-R (OreR) strain was used as the wild type. 1×*bcd* strain (*+/CyO-bcd+*; *E1s*) was developed previously (Liu and Ma, 2013) and was obtained as a gift from Dr. Jun Ma (Zhejiang University). *hb*-BAC reporter constructs were previously developed (Perry et al., 2011). The distal-

enhancer-removed BAC construct and its control were obtained as gifts from Dr. Michael Perry (University of California San Diego) and Dr. Alistair Boettiger (Stanford University). The proximal-enhancer-removed construct and its control were rebuilt as previously described (Perry et al., 2011). Transgenes in these constructs were constructed from BAC CH322-55J23 (Pare et al., 2009), which contains a 20-kbp *Drosophila* genomic sequence encompassing the *hb* gene and its proximal and distal enhancers. A *yellow-kanamycin* fusion was used to replace the *hb* CDS in all BACs, while the proximal or distal enhancers in the BACs were substituted with *ampicillin*. All BACs were integrated on chromosome 2 of *Drosophila*. The distal-enhancer-removed transgene and its control were integrated into landing site VK37 (Bloomington Stock Center number 24872). The proximal-enhancer-removed transgene and its control were integrated into landing site attP40 (Bloomington Stock Center number 25709).

METHOD DETAILS

smFISH probe design

Sets of DNA oligonucleotides complementary to the target transcripts (nine probes for *hb* P1 5'UTR, 32 probes for *hb* P1 intron, 48 probes for *hb* CDS, eight probes for *hb* P2 3'UTR, and 43 probes for *yellow*) were designed (Table S1) and synthesized (Biosearch Technologies). Each probe was ordered with a 3' amine group (mdC(TEG-Amino)) and was conjugated to various fluorophores, as described previously (Skinner et al., 2013; Xu et al., 2015). *hb* P1-5'UTR and intron probes were conjugated with tetramethylrhodamine (TAMRA; Thermo Fisher Scientific, C6123). *hb* P2-3'UTR and *yellow* probes were conjugated with Alexa Fluor™ 647 (Invitrogen, A20106). *hb* CDS probes were conjugated with either Alexa Fluor™ 647 (Invitrogen, A20106) or Alexa Fluor™ 488 (Invitrogen, A20100).

Embryo staining

Embryo collection, fixation, and labeling were performed according to a previously published

protocol (Xu et al., 2015). Briefly, 2-hour-old embryos were collected at 25°C, fixed with 4% paraformaldehyde solution, and stored in 100% methanol at −20°C. For smFISH, fixed embryos were rehydrated (4 × 10 min) in PBTx (1× PBS, 0.1% (v/v) Triton X-100) at room temperature, washed (2 × 10 min) in hybridization wash buffer at 30°C, and incubated with the probe-containing hybridization buffer (2× SSC, 20% (w/v) formamide, 0.1% (v/v) Triton X-100) at 30°C overnight. After hybridization, embryos were washed in hybridization wash buffer at 30°C (2 × 10 min) and in 2× SSC at room temperature (2 × 10 min). For immunofluorescence (IF), embryos were washed (4 × 10 min) in PBTx and blocked in PBT-B (1× PBS, 20% (v/v) western blocking reagent (Roche, 11921673001), 2 mM ribonucleoside vanadyl complex (NEB, S1402S), 0.1% (v/v) Triton X-100) at room temperature for 1 h. The preabsorbed rabbit anti-Bcd primary antibody (Santa Cruz Biotechnology, SC-66818) was incubated with embryos at 4°C for 20 h. Following primary antibody staining, embryos were further washed (4 × 10 min) in PBTx, blocked in PBT-B at room temperature for 1 h, and incubated with goat anti-rabbit IgG secondary antibodies conjugated with Alexa Fluor™ 488 (Invitrogen, A11008) at room temperature for 1 h. For DNA counterstaining, embryos were washed (4 × 10 min) in PBTx and stained with Hoechst 33342 at room temperature for 10 min. Following additional washes (4 × 10 min) in PBTx, embryos were mounted in Aqua-Poly/Mount (Polysciences, 18606). Imaging was performed after the samples were completely solidified.

Imaging

Most embryos were imaged using a Zeiss LSM 880 laser scanning confocal microscope equipped with a GaAsP detector and a 63× oil-immersion objective (1.4 NA). 16-bit image stacks were acquired with a pixel size of 71 × 71 nm^2 and a z-step size of 0.32 μm. A small number of embryos (n = 5) were imaged using a Leica TCS SP8 confocal microscope equipped with a GaAsP detector and a 63× oil-immersion objective (1.4 NA). 12-bit image stacks were acquired with a pixel size of 81 × 81 nm^2 and a z-step size of 0.3 μm. Nc11–13 embryos at the mitotic interphase were selected based on the number and shape of the nuclei (Hoechst signal). Approximately 10 μm of

the cortex layer of each embryo was imaged.

Preprocessing and nuclear segmentation

Image processing and data analysis followed a previously developed pipeline (Xu et al., 2015) with updated algorithms to improve accuracy and efficiency. Briefly, raw images were divided by a normalized flat-field image to correct for monochromatic aberrations. Three-dimensional (3D) segmentation of nuclei from the Hoechst image stack was done using a combination of local threshold (to optimize a circularity parameter) and watershed (to separate the merged nuclei). The nuclear cleavage cycle of the embryo was determined by the number of recognized nuclei. Embryo boundary was identified from the averaged Hoechst image by thresholding image pixels outside the nuclear area. This boundary was then used to determine the AP position of each nucleus.

mRNA quantification

For mRNA quantification, spot candidates in smFISH images were identified as 3D local maxima in the image stack. Since the splicing process occurs inside the nucleus, intron spot candidates were only identified in the nuclear region. The local intensity profile of each candidate was fitted to a two-dimensional (2D) Gaussian function to extract the peak height (I_{peak}) and radius (σ_0). The spot intensity was calculated as $I = 2\pi I_{peak}\sigma_0^2$. By comparing the joint distribution of peak height and radius between the anterior and posterior spots, a 2D threshold was determined to distinguish real mRNA spots from background noise. The typical intensity, I_0, of a single mRNA molecule was extracted by fitting the primary peak of the spot intensity distribution to a multi-Gaussian function. A threshold of $3I_0$ was defined to identify sites of active transcription from mRNA spots inside each nucleus. The equivalent number of nascent transcripts at each transcription site was estimated by dividing the intensity of the transcription site by I_0.

To identify signals corresponding to the same *hb* locus in two different smFISH channels, we calculated the mutual distance between every possible pair of active transcription sites detected

in different smFISH channels. The distribution of all the mutual distances in an embryo exhibited two distinct populations. Using a threshold distance of 0.55 μm, the colocalized pairs of active transcription sites were identified. Each pair corresponded to a single *hb* locus. In contrast, each of the unpair active transcription sites belonged to a different *hb* locus, whose activity in the other smFISH channel was zero.

In some anterior nuclei, three or four bright FISH spots appeared because of the replication of the *hb* gene (Little et al., 2013) (Figure S1A). To identify nascent mRNA signals corresponding to sister loci pairs, we calculated the mutual distance between every possible pair of active transcription sites in each nucleus. The distribution of all the mutual distances in the embryo exhibited two distinct populations. Using a threshold distance of 0.71 μm, sister loci pairs were distinguished from unpaired homologous loci.

Protein quantification

For protein quantification, the average immunofluorescence (IF) intensity of each nucleus was calculated from the central *z*-slice of the nucleus. IF spots in the cytoplasm were identified and quantified to determine the typical intensity, I_1, of a single protein molecule, following the same procedure used for the smFISH signal. The absolute protein concentration of a nucleus was estimated by dividing the average IF intensity of the nucleus by $(2\pi)^{1/2}\sigma_z I_1$, where σ_z is the half-width of the single-protein intensity profile in the *z* dimension.

In the preceding steps, nuclear segmentation, embryo boundary identification, and detection of active transcription sites could be further refined and corrected manually using custom MATLAB graphical user interfaces.

Measuring the spatial profile of promoter activity

We analyzed the expression profile of a promoter using embryos in the mid-to-late mitotic

interphase to ensure steady-state promoter activity. To identify silent loci (no nascent mRNA) in the embryo, we assumed that each nucleus had two (for nuclei containing ≤2 active transcription sites) or four (for nuclei containing >2 active transcription sites) *hb* loci. The number of silent loci was estimated accordingly. For each embryo, we plotted the number of nascent mRNAs (r) against nuclear position (x) for all loci and binned individual data points by x. Within the range of 0.25–0.75 EL, we used a least-square algorithm to fit the binned data to a logistic function:

$$r = r_{\max} \frac{e^{-(x-x_0)/d}}{e^{-(x-x_0)/d} + 1} + r_0 \quad (4)$$

where x_0 is the boundary position of the expression domain, d is the half-width of the transition region, $r_{\max}$ is the maximal transcription level induced in the anterior region, and r_0 denotes the basal activity in the posterior part.

Measuring the fluctuation of promoter activity

At the single-molecule level, gene expression constantly varies over time and between different cells. Based on the correlation between the homologous loci in the same cell, the fluctuation or noise of gene expression may be divided into two parts: the intrinsic noise due to the inherent stochasticity of biochemical reactions and the extrinsic noise caused by cell-to-cell variability of the microenvironment (Elowitz et al., 2002). Previous studies have shown that *hb* expression in the early embryo is intrinsically stochastic and bursty (Little et al., 2013; Xu et al., 2015; Zoller et al., 2018).

To characterize the expression variability of different *hb* promoters, we computed, for each promoter, the Fano factor (F) of nascent mRNA copy number (r) per locus in the anterior expression domain (0.2–0.4 EL) (Hortsch and Kremling, 2019; Ozbudak et al., 2002; Xu et al., 2015):

$$F = \frac{\sigma^2}{\langle r \rangle} \tag{5}$$

where $\langle r \rangle$ and σ are the mean and standard deviation of the single-locus data, respectively. The Fano factors of P1- and P2-specific signals were much larger than one (Figure 1H), indicating bursty transcription from both promoters (Raj et al., 2006; Sanchez and Golding, 2013).

We quantified the intrinsic noise of P1 and P2 expression in the anterior expression domain (0.2–0.4 EL) of an embryo using the following formula (Waymack et al., 2020):

$$\eta^2 = \frac{\langle (m_1 - m_2)^2 \rangle}{2\langle m_1 \rangle \langle m_2 \rangle} \tag{6}$$

where m_1 and m_2 are the nascent mRNA signals at two homologous loci in the same nucleus measured using a given probe set, respectively.

Measuring the correlation between promoter loci

To distinguish the intrinsic and extrinsic noise of different promoter activities, we computed the correlation coefficient (ρ) of the nascent mRNA copy number between the two homologous copies of a given promoter within the same nucleus. Specifically, we divided the single-locus data of the promoter activity (equivalent number of nascent mRNA) in an embryo into two groups, r_1 and r_2. Each group corresponded to one of the two homologous loci in the nucleus. In a given region of the embryo, we applied the following formula:

$$\rho = \frac{\langle (r_1 - \langle r_1 \rangle) \cdot (r_2 - \langle r_2 \rangle) \rangle}{\sigma_1 \sigma_2} \tag{7}$$

where $\langle r_1 \rangle$, $\langle r_2 \rangle$, σ_1, and σ_2 are the mean and standard deviation of each group, respectively. ρ may

be considered weak if its absolute value is below 0.3 (Mukaka, 2012). In the anterior expression domain (0.2–0.4 EL), P1, P2, and CDS signals showed little correlation (<0.15, Figure S1C), agreeing with previous reports of loci independence (Little et al., 2013; Xu et al., 2015). Thus, intrinsic noise dominates P1 and P2 expression. To further evaluate the interaction between the two promoters, we computed the correlation coefficient between P1 and P2 signals from the same (intra-allele) or different (inter-allele) *hb* loci in the nucleus using the same formula, where r_1 and r_2 denote the activities of individual P1 and P2 copies, respectively. Both quantities were at low levels (<0.06, Figure S1D), indicating that the two promoters do not interact during expression.

Estimating promoter contributions to *hb* activity

To estimate the contribution of P1 and P2 activities to nascent *hb* transcription, we co-labeled fly embryos with P1-5'UTR, P2-3'UTR, and CDS probes (Figure 2A). For P1- and P2-active *hb* loci in the position range of 0.2–0.7 EL of an embryo, we plotted the three FISH signals (in units of the number of nascent mRNAs) against each other (Figure 2B). We applied linear regression to fit the single-locus data to **Equation (1)**. With the inferred a_1 and a_2 values, we computed the P1 contribution to the average nascent CDS signal as

$$f_{\text{P1-CDS}} = \frac{a_1 r_{\text{P1}}}{r_{\text{CDS}}} \tag{8}$$

where r_{CDS} and r_{P1} are the average nascent CDS and P1-5'UTR signals per *hb* locus, respectively. The rest of the nascent CDS signal should come from P2. However, directly computing the P2 contribution using a similar formula revealed an extra component in the nascent CDS signal that was not labeled by promoter-specific probes (Figures S2B). In the anterior expression domain, this component corresponded to >20% of the nascent CDS signal (Figures S2C). This phenomenon agrees with our observation that some CDS-positive *hb* loci lack P1-5'UTR and P2-3'UTR signals. To determine the origin of this extra component, we fitted its expression profile to

a logistic function. The estimated expression boundary position (x_0 = 0.47 EL ± 0.02 EL) matched the P2-3'UTR signal (Figure S2D), indicating that the component is from P2 transcription. The P2-specific probes failed to label this component because the probes target the 3'UTR of *hb*-RA. It could be that mRNA termination complexes on the 3' UTR block FISH probes from binding (Bentley, 2014). Moreover, a previous study reported alternative termination of *hb* transcription (Bender et al., 1988), which may account for unlabeled P2 transcripts. By summing the contributions from labeled and unlabeled P2 transcripts, we decomposed the CDS profile into different promoter activities (Figure 2E and 2F).

To compute promoter contributions to the intrinsic noise of nascent *hb* transcription, we estimated $\eta^2_{\text{P1-CDS}}$ in **Equation (3)** from the intrinsic noise of the nascent P1-5'UTR signal (see *Mathematical modeling of transcriptional kinetics* of STAR Methods). The contribution of P1 to the intrinsic noise of nascent CDS signal was calculated as:

$$w_{\text{P1-CDS}} = \frac{\eta^2_{\text{P1-CDS}} f^2_{\text{P1-CDS}}}{\eta^2_{\text{CDS}}} \tag{9}$$

The rest of the intrinsic noise was contributed by P2.

Measuring the gene regulation function (GRF)

To analyze the regulation of a promoter by Bcd, we plotted, for each embryo, the nascent mRNA signal of each gene locus versus the nuclear Bcd concentration within the position range of 0.25–0.75 EL. To extract the GRF, we binned individual data points by Bcd concentration and fitted them to a Hill function using a least-squares algorithm:

$$y = a\frac{[\text{Bcd}]^h}{[\text{Bcd}]^h + C_0^h} + d \tag{10}$$

where h is the Hill coefficient, C_0 is the concentration threshold for promoter activation, a indicates the maximal level of Bcd-dependent activity, and d denotes the basal activity.

Measuring Bcd binding

To quantify Bcd binding at a specific *hb* promoter, we used active P1 and P2 transcription sites to locate individual (active) promoter loci. Near each locus, a "locus-integration region" (*xy* distance ≤ 3 pixel and *z* distance = 0 from the locus) and an "out-of-locus region" (*xy* distance ≤ 6 pixels and ≥ 3 pixels, *z* distance = 0) were defined, which covered the nuclear volumes of V_I and V_o, respectively. The nuclear IF signal (in units of the number of Bcd molecules) within these two regions was integrated and denoted as I_I and I_o, respectively. The enriched Bcd signal was defined as the difference between I_I and I_o in consideration of the volume difference between the two regions, i.e., $I_{enrich} = I_I - I_o \cdot V_I / V_o$. Data from multiple embryos in the sample nuclear cycle were pooled to increase the sample size. Data in the nuclear position range of 0.2–0.35EL were averaged to estimate the mean Bcd binding level of the anterior expression domain. To plot the Bcd binding curve, we binned the single-locus data by nuclear position and related mean Bcd enrichment with mean nuclear position or Bcd concentration.

Mathematical modeling of transcriptional kinetics

Model selection

Transcription kinetics determines the distribution of nascent mRNA copy number on individual gene loci. Specifically, bursty gene expression often results in a multimodal distribution (Munsky et al., 2012; Zenklusen et al., 2008). A widely used model for describing bursty gene expression is the two-state telegraph model (Peccoud and Ycart, 1995; Raj et al., 2006; Senecal et al., 2014; Xu et al., 2016; Zenklusen et al., 2008), in which the gene randomly switches between an inactive and an active transcription state. If transitions between states are slower than the residence time of nascent mRNA on the transcription site, the nascent mRNA distribution predicted from the

model exhibits two Poissonian peaks (Xu et al., 2016). Generalizing the model to include more states can create more peaks in the distribution. In general, the number of peaks (i.e., modality) of the experimentally observed distribution sets the minimum number of gene states required for modeling the transcription process.

In this study, the distributions of P1 and P2 nascent mRNA signals both exhibited trimodal distributions (Figure 5A). One peak in the distribution corresponds to silent loci (m = 0), while two other peaks correspond to two groups of active loci with different expression levels. There are two possible explanations for this phenomenon: (1) individual promoters perform three-state transcription kinetics, and (2) each observed promoter locus is composed of a pair of closely located sister loci that are indistinguishable under the microscope (Little et al., 2013; Zoller et al., 2018). To evaluate these two explanations, we plotted the distribution of nascent mRNA signals measured from optically resolved sister loci pairs (Figure 5B). For each promoter, the sister loci exhibited two active populations. The distribution was well fitted by a sum of two Poisson distributions (Considering the intensity threshold used for identifying active transcription sites, the very left part of the distribution (<3 mRNAs) was neglected). By comparing the weights of the two Poisson peaks, we showed that the minor population in the distribution corresponds to 38.4% ± 3.3% of P1 and 17.0% ± 6.1% of P2 sister loci (mean ± s.e.m., data from seven embryos at nc13). Thus, the activity of a single promoter needs to be described with at least three transcription states.

Model assumptions

The nascent transcription of each promoter locus was modeled as a three-state process. The model considers three transcription states of the promoter: an “OFF” state (denoted as state 0), where the promoter is transcriptionally inactive, and two “ON” states (denoted as states 1 and 2), where the promoter actively initiates new transcripts. State transitions and mRNA initiations are assumed to be Poisson processes with specific rates k_{ij} and $k_{\mathrm{INI},i}$ (i, j = 0, 1, 2), respectively. Following initiation, each nascent mRNA molecule elongates to the final length L with a constant

speed V_{EL}. Once completed, the mRNA resides on the gene for an extra termination period, T_R, before being released.

At a given observation time, the state of the system at a given observation time t_{ob} is determined by the promoter state n (n = 0, 1, 2) and the total signal of nascent mRNA m ($m \geq 0$). Since a nascent mRNA molecule stays on the gene for a fixed period $T_{RES} = L/V_{EL} + T_R$, m is the sum of signals from all transcripts initiated between $t_{ob} - T_{RES}$ and t_{ob}, i.e., $m = \sum_{-T_{RES} \leq \tau \leq 0} g(\tau)$. Here, $\tau = t - t_{ob}$ is the time relative to t_{ob}. Considering that nascent transcripts may be incomplete, we defined a contribution function $g(\tau)$ to describe the signal from a transcript initiated at time τ (Senecal et al., 2014; Xu et al., 2016). $g(\tau)$ varies between zero and one, and its exact shape depends on the target positions of the probe set and the magnitude of T_R. The shape of $g(\tau)$ for each probe set is shown in Figure S2A.

Master equation

We wrote a master equation for the probability distribution of (n, m) as

$$\frac{d\mathbf{P}(m)}{d\tau} = (\mathbf{K} - \mathbf{K}_{INI})\mathbf{P}(m) + \mathbf{K}_{INI}\mathbf{P}(m - g(\tau)) \quad (11)$$

where $\mathbf{P}(m) = \begin{bmatrix} P(0,m) \\ P(1,m) \\ P(2,m) \end{bmatrix}$ is the probability distribution vector, $\mathbf{K} = \begin{bmatrix} -k_{01} - k_{02} & k_{10} & k_{20} \\ k_{01} & -k_{10} - k_{12} & k_{21} \\ k_{02} & k_{12} & -k_{20} - k_{21} \end{bmatrix}$ and $\mathbf{K}_{INI} = \begin{bmatrix} 0 & 0 & 0 \\ 0 & k_{INI,1} & 0 \\ 0 & 0 & k_{INI,2} \end{bmatrix}$ are matrices describing the promoter-state transition and transcription initiation, respectively (Xu et al., 2015; Xu et al., 2016). Assuming that the marginal distribution of the promoter state at $\tau = -T_{RES}$ is $q(n)$, we can apply an initial condition of $\mathbf{P}(m) = q(n)\delta_{m,0}$ to solve **Equation (11)** for $\mathbf{P}(m)$ at τ = 0. Specifically, $q(n)$ at steady state satisfies $\mathbf{Kq} = 0$.

The general three-state model allows direct transitions between any two states ($k_{ij} > 0$ for all i and j). However, most gene regulation models to date followed the thermodynamic formalism with a detailed balance between states (Mahan, 1975). This constraint limits the topology of the state-transition diagram, i.e., transitions between certain states may be forbidden. Specifically, a three-state model with detailed balance needs to satisfy one of the two schemes of promoter activation, i.e., the sequential activation scheme, in which transitions between states 0 and 2 are forbidden, and the parallel activation scheme, where transitions between states 1 and 2 are not allowed (Figure S5A).

Mean, variance, and noise

The mean signal of the nascent mRNA may be derived from **Equation (11)** as follows (Xu et al., 2016):

$$\langle m \rangle = \mathbf{u}\left\{\int_{-T_{\mathrm{RES}}}^{0} g(\tau)\mathbf{W}(\tau)d\tau\right\}\mathbf{q} \tag{12}$$

where $\mathbf{u}$ = (1, 1, 1) and $\mathbf{W}(\tau) = e^{-\mathbf{K}\tau}\mathbf{K}_{\mathrm{INI}}e^{\mathbf{K}\tau}$. At steady state, the magnitude of $\langle m \rangle$ is proportional to the mean of the contribution function, i.e.,

$$\langle m \rangle = \mathbf{u}\mathbf{K}_{\mathrm{INI}}\mathbf{q}\int_{-T_{\mathrm{RES}}}^{0} g(\tau)d\tau \tag{13}$$

Thus, the mean nascent mRNA signals measured using different probe sets are in proportion, i.e.

$$\frac{\langle m_1 \rangle}{\langle m_2 \rangle} = \frac{\overline{g_1}}{\overline{g_2}} \tag{14}$$

where $\bar{\cdot} = \frac{1}{T_{\mathrm{RES}}}\int_{-T_{\mathrm{RES}}}^{0} \cdot\, d\tau$ denotes time averaging. A probe set targeting the 5' region of a transcript should, on average, produce more signal (in units of the number of Bcd molecules) than

a probe set targeting the 3' region of the same transcript. In our study, the ratios between the CDS and promoter-specific signals were defined as a_1 and a_2 in **Equation (1)**. $a_1 < 1$ and $a_2 > 1$ are consistent with the relative target positions of the different probe sets in mRNA sequences.

Moreover, the ratio between different probe signals is quantitatively related to T_R, i.e.

$$\frac{\langle m_1 \rangle}{\langle m_2 \rangle} = \frac{\overline{g_{10}} \cdot L + T_R V_{EL}}{\overline{g_{20}} \cdot L + T_R V_{EL}} \tag{15}$$

where g_{10} and g_{20} are the contribution functions for probe sets 1 and 2 with $T_R = 0$. Considering an mRNA elongation speed V_{EL} = 1.5 kb/min (Garcia et al., 2013), we estimated from a_1 = 0.53 and a_2 = 2.74 that T_R = 142 s for P1 and T_R = 46 s for P2.

Unlike probes targeting the exon or UTR regions of a transcript, the intron probe signal is affected by co-transcriptional splicing (Figure 2D). Assuming a Poissonian slicing process occurring after the completion of intron synthesis with specific rate $k_{splicing}$, we wrote the average nascent intron signal per locus as

$$\langle m \rangle = \mathbf{u}\mathbf{K}_{INI}\mathbf{q}\int_{-T_{RES}}^{0} g(\tau)s(\tau)d\tau \tag{16}$$

where $s(\tau)$ is the intron survival probability (without being spliced) for a nascent transcript initiated at time τ. $s(\tau)$ is a simple piecewise function satisfying

$$s(\tau) = \begin{cases} 1, & \tau > -L_{5'\text{-intron}} / V_{EL} \\ e^{k_{splicing}(\tau + T_{5'\text{-intron}})}, & \tau \le -L_{5'\text{-intron}} / V_{EL} \end{cases} \tag{17}$$

with $L_{5'\text{-intron}}$ denoting the sequence length from the 5' cap to the end of the intron. Thus, the mean nascent P1-intron and 5'UTR signals should be in proportion, with the ratio depending on $k_{splicing}$. The experimental data confirmed this linear relationship and suggested a ratio is of 0.59 (Figure S2E). Assuming that V_{EL} = 1.5 kb/min (Garcia et al., 2013) and $T_{R\text{-}P1}$ = 142 s, we estimated that

$k_{splicing}$ = 175 s^{-1}. The time scale is similar to that observed in other genes (Audibert et al., 2002; Bentley, 2014; Schmidt et al., 2011; Singh and Padgett, 2009).

The variance of the nascent mRNA signal was derived from **Equation (11)** as (Xu et al., 2016):

$$\sigma_m^2 = \mathbf{u}\cdot\left\{\int_{-T_{RES}}^{0} d\tau_1 g(\tau_1)^2 \mathbf{W}(\tau_1)\right\}\mathbf{q} + 2\mathbf{u}\cdot\left\{\int_{-T_{RES}}^{0} d\tau_1 \int_{-T_{RES}}^{\tau_1} d\tau_2 g(\tau_1)g(\tau_2)\mathbf{K}_{INI}\left(e^{\mathbf{K}(\tau_1-\tau_2)} - \mathbf{qu}\right)\mathbf{K}_{INI}\right\}\mathbf{q} \quad (18)$$

In case of slow gene-state transitions, $e^{\mathbf{K}(\tau_1-\tau_2)} \approx \mathbf{I}$. Thus,

$$\sigma_m^2 \approx \mathbf{uK}_{INI}\mathbf{q}\int_{-T_{RES}}^{0} g(\tau)^2 d\tau + \mathbf{uK}_{INI}\left(\mathbf{I}-\mathbf{qu}\right)\mathbf{K}_{INI}\mathbf{q}\left(\int_{-T_{RES}}^{0} g(\tau)d\tau\right)^2 \quad (19)$$

Combining **Equations (13)** and **(19)**, we wrote the noise of the nascent mRNA signal as

$$\eta^2 = \frac{\sigma_m^2}{\langle m\rangle^2} = \frac{1}{\langle m\rangle}\frac{\overline{g^2}}{\bar{g}} + \frac{\mathbf{uK}_{INI}\left(\mathbf{I}-\mathbf{qu}\right)\mathbf{K}_{INI}\mathbf{q}}{\left(\mathbf{uK}_{INI}\mathbf{q}\right)^2} \quad (20)$$

The first term in **Equation (20)** indicates Poisson noise, which is inversely proportional to $\langle m\rangle$. Its magnitude varies with the shape of *g*. The second term in **Equation (20)** is due to bursty expression, and the magnitude is invariant with the shape of *g*. For brevity, we rewrote the expression of noise as

$$\eta^2 = \frac{S_g}{\langle m\rangle} + \eta_{burst}^2 \quad (21)$$

where $S_g = \overline{g^2}/\bar{g}$ is a constant for a given probe set and mRNA species. For P1-specific transcripts, we had $S_{P1\text{-}CDS}$ = 0.78 for the CDS probes and $S_{P1\text{-}5'UTR}$ = 0.99 for the 5'UTR probes.

Numerically solving the master equation

Because the analytical solution for **Equation (11)** is not available, we solved the equation numerically using the finite state projection (FSP) method (Munsky and Khammash, 2008; Neuert et al., 2013; Xu et al., 2015). Briefly, we discretized and truncated the range of nascent mRNA signal to $m = 0, \Delta m, 2\Delta m, \ldots, m_{\max}$, with $\Delta m \ll 1$ and $m_{\max}$ large enough to cover the main portion of the nascent mRNA distribution. **Equation (11)** then transforms to a finite-dimension version:

$$\dot{\bar{\mathbf{P}}} = \left(\bar{\mathbf{K}} + \bar{\mathbf{K}}_{\mathrm{INI}}(\tau)\right)\bar{\mathbf{P}} = \begin{bmatrix} \mathbf{K}-\mathbf{K}_{\mathrm{INI}} & 0 & 0 & 0 \\ 0 & \mathbf{K}-\mathbf{K}_{\mathrm{INI}} & 0 & \cdots \\ 0 & 0 & \mathbf{K}-\mathbf{K}_{\mathrm{INI}} & \cdots \\ \vdots & \vdots & \vdots & \ddots \\ \mathbf{K}_{\mathrm{INI}} & 0 & 0 & \ddots \\ 0 & \mathbf{K}_{\mathrm{INI}} & 0 & \ddots \\ 0 & 0 & \mathbf{K}_{\mathrm{INI}} & \ddots \\ \vdots & \vdots & \vdots & \ddots \end{bmatrix} \begin{bmatrix} \mathbf{P}(0) \\ \mathbf{P}(\Delta m) \\ \mathbf{P}(2\Delta m) \\ \vdots \\ \mathbf{P}(g(\tau)) \\ \mathbf{P}(g(\tau)+\Delta m) \\ \mathbf{P}(g(\tau)+2\Delta m) \\ \vdots \end{bmatrix}, \tag{22}$$

where $\bar{\mathbf{K}} = \begin{bmatrix} \mathbf{K} & 0 & 0 & \cdots \\ 0 & \mathbf{K} & 0 & \cdots \\ 0 & 0 & \mathbf{K} & \cdots \\ \vdots & \vdots & \vdots & \ddots \end{bmatrix}$, $\bar{\mathbf{K}}_{\mathrm{INI}}(\tau) = \begin{bmatrix} -\mathbf{K}_{\mathrm{INI}} & 0 & 0 & \cdots \\ 0 & -\mathbf{K}_{\mathrm{INI}} & 0 & \cdots \\ \vdots & 0 & -\mathbf{K}_{\mathrm{INI}} & \cdots \\ \mathbf{K}_{\mathrm{INI}} & \vdots & 0 & \cdots \\ 0 & \mathbf{K}_{\mathrm{INI}} & \vdots & \ddots \\ 0 & 0 & \mathbf{K}_{\mathrm{INI}} & \ddots \\ \vdots & \vdots & \vdots & \ddots \end{bmatrix}$.

Next, we discretized the time range $\tau \in [-T_{\mathrm{RES}}, 0]$ into a series with $\Delta\tau \ll T_{\mathrm{RES}}$. The probability distribution of (n, m) at $\tau = 0$ was computed by propagating the initial state $\bar{\mathbf{P}}_{\tau=-T_{\mathrm{RES}}}$ through the series, i.e.,

$$\bar{\mathbf{P}}_{\tau=0} = \left(\mathbf{I} + \bar{\mathbf{K}}\Delta\tau + \bar{\mathbf{K}}_{\mathrm{INI}}(-\Delta\tau)\Delta\tau\right)\cdots\left(\mathbf{I} + \bar{\mathbf{K}}\Delta\tau + \bar{\mathbf{K}}_{\mathrm{INI}}(-T_{\mathrm{RES}})\Delta\tau\right)\bar{\mathbf{P}}_{\tau=-T_{\mathrm{RES}}}, \tag{23}$$

where **I** is the unit matrix. In this paper, we used $\Delta m = 0.1$ and $\Delta\tau = T_{RES}/2000$ to balance the accuracy and speed of computation.

Modeling the DNA replication effect

The fact that some anterior nuclei contain more than two bright FISH spots (Figure S1A) indicates that the *hb* gene in the imaged embryo may have been replicated. Thus, many of the observed bright FISH spots may indeed be a pair of closely located sister loci that are indistinguishable under the microscope (Little et al., 2013; Zoller et al., 2018). To consider this effect in the model/analysis, we note that the two sister gene copies are expressed independently (Little et al., 2013; Zoller et al., 2018). The distribution of the total signal from two closely located sister loci should be a convolution of that of individual ones, i.e.,

$$P(m_{ob}) = P(m_{single}) * P(m_{single}) \tag{24}$$

where $P(m_{ob})$ is the probability of the observed signal from a bright FISH spot composed of two closely located sister loci, and $P(m_{single})$ denotes the nascent mRNA distribution of a single gene copy computed from the model.

In addition to the probability distribution, the low-order statistics of the observed bright FISH spot are also affected by gene replication. Specifically, the mean and variance double with gene replication, while the Fano factor and correlation coefficient stay unchanged.

Inferring the transcription kinetics

We fitted the experimental data to estimate the kinetic parameters of each promoter using the maximum likelihood estimation (MLE) method (Neuert et al., 2013; Xu et al., 2015). Briefly, we divided the single-locus data of nascent mRNAs from an embryo into multiple subsets according to the nuclear position. To ensure a sufficient number of data points in each subset, we used

overlapping binning with a bin size of 0.1 EL. For a given parameter set $\tilde{\mathbf{K}} = \{k_{ij}, k_{\mathrm{INI},i}\}$, the likelihood of observing a subset of data is

$$L(M \mid \tilde{\mathbf{K}}) = \prod_i P(m_i \mid \tilde{\mathbf{K}}) \tag{25}$$

where $P(m_i \mid \tilde{\mathbf{K}})$ is the probability of observing m_i nascent mRNAs given $\tilde{\mathbf{K}}$. For each subset m_i, we searched $\tilde{\mathbf{K}}$ to maximize the likelihood in a broad range of parameter values (k_{ij} from 0 to 10 min^{-1}, $k_{\mathrm{INI},i}$ from 0 to 100 min^{-1}).

To increase the efficiency and robustness of the parameter search for a three-state model, we first fitted a data set pooled from multiple embryos in the same nuclear cycle. For each nuclear position bin, we compared two types of models with either sequential or parallel activation schemes. Using a combination of simplex and simulated annealing methods for the parameter search, we determined that both P1 and P2 data were better fitted by the sequential activation model for all nuclear position bins. Moreover, the results showed that Bcd mainly affected promoter activation rates, while the inactivation and transcription initiation rates remained stable (Figure S5B). Thus, we fixed promoter inactivation and transcription initiation rates at their mean values and re-scanned the activation rates in detail. Once all kinetic rates were determined for the pooled data set, we applied them as initial values to fit the single-embryo data. To increase the accuracy of simplex and simulated annealing methods in the above steps, we repeated each search 12 times. The result with the highest likelihood was chosen.

Describing P1 and P2 activities using a single model

Our results showed that P1 and P2 followed common three-state transcription kinetics driven by the same set of Bcd binding events at the two enhancers. Thus, we can combine the description of the two promoters into a single model to relate Bcd binding configurations with P1 and P2

transcription kinetics (Figure 5I).

The first part of the model describes the Bcd binding dynamics. There are many Bcd binding sites on the proximal and distal enhancers (Driever and Nusslein-Volhard, 1989; Perry et al., 2011; Struhl et al., 1989). For simplicity, we assumed that Bcd binding at each enhancer was highly cooperative, with all binding sites being occupied/emptied in one step. This assumption resulted in four possible Bcd binding configurations (Figure 5I). In the canonical framework of transcription factor binding dynamics, transitions between these binding configurations are described as Poisson processes, whose kinetic rates are related to Bcd concentration by a power law (Estrada et al., 2016). The steady-state probability of each binding configuration (s) satisfies a rational function,

$$P_s(C_{\mathrm{Bcd}}) = \frac{r_s C_{\mathrm{Bcd}}^{n_s}}{\sum_s r_s C_{\mathrm{Bcd}}^{n_s}} \tag{26}$$

where C_{Bcd} is the Bcd concentration, n_s and r_s are the power-law exponents and proportionality constants for configuration s, respectively. Specifically, the configuration with no Bcd bound at either enhancer, (typically denoted as $s = 0$) satisfies $n_0 = 0$ and $r_0 = 1$. For an equilibrium system satisfying detailed balance (Mahan, 1975), n_s equals the number of bound Bcd molecules. For a nonequilibrium system, n_s may take higher values (Estrada et al., 2016), yet the general form of **Equation (26)** still holds.

To relate Bcd binding with the transcriptional activity of a promoter, we assumed that transitions between different promoter states were triggered by specific Bcd binding configurations (Figure 5I). Bcd binding at a single enhancer (proximal or distal) triggers the transition of a promoter from state 0 to state 1, while the binding at both enhancers triggers the transition from state 1 to state 2. Strictly speaking, these transitions can only happen when the system is at given Bcd binding configurations. However, since transcription factor binding and unbinding happen at a much faster time scale than promoter activation (Zoller et al., 2018), the

promoter activation rates (k_{01} and k_{12}) can be modeled as constants over time.

In a simple model, the promoter activation rate may be proportional to the probability of the corresponding Bcd binding configuration. However, activation of a real promoter involves a series of molecular events, some of which are independent of Bcd (Xu et al., 2015; Zoller et al., 2018). The activation rate estimated from nascent mRNA distribution (k_{01} or k_{12}) represents the overall time scale of all molecular events, i.e.,

$$\begin{cases} k_{01}^{-1} = \left[a_1 P_1(C_{\mathrm{Bcd}}) + a_2 P_2(C_{\mathrm{Bcd}})\right]^{-1} + \tau_{01} \\ k_{12}^{-1} = \left[b P_3(C_{\mathrm{Bcd}})\right]^{-1} + \tau_{12} \end{cases} \tag{27}$$

where a and b are proportionality constants and s = 1, 2, 3 denote the binding configurations with Bcd bound at the proximal, distal, or both enhancers, respectively. τ represents the time scale of Bcd-independent molecular events, which can saturate k_{01} and k_{12} at high Bcd concentration. **Equation (27)** explains the Hill-function-like relationship between promoter activation rates (k_{01} and k_{12}) and Bcd concentration observed in Figure 5C.

Since P1 and P2 nascent mRNA signals have little correlation (Figure S1D), we speculated that the activation of the two promoters was triggered independently. Thus, the joint distribution of P1 and P2 nascent mRNA signals is the product of their marginal distributions (Figure 5J).

REFERENCES

Audibert, A., Weil, D., and Dautry, F. (2002). In vivo kinetics of mRNA splicing and transport in mammalian cells. Mol. Cell. Biol. *22*, 6706-6718.

Benabdallah, N.S., Williamson, I., Illingworth, R.S., Kane, L., Boyle, S., Sengupta, D., Grimes, G.R., Therizols, P., and Bickmore, W.A. (2019). Decreased Enhancer-Promoter Proximity Accompanying Enhancer Activation. Mol.

Cell *76*, 473-484.

Bender, M., Horikami, S., Cribbs, D., and Kaufman, T.C. (1988). Identification and expression of the gap segmentation gene hunchback in Drosophila melanogaster. Dev. Genet. *9*, 715-732.

Bentley, D.L. (2014). Coupling mRNA processing with transcription in time and space. Nat. Rev. Genet. *15*, 163-175.

Berry, S., Dean, C., and Howard, M. (2017). Slow Chromatin Dynamics Allow Polycomb Target Genes to Filter Fluctuations in Transcription Factor Activity. Cell Syst. *4*, 445-457.

Bintu, L., Yong, J., Antebi, Y.E., McCue, K., Kazuki, Y., Uno, N., Oshimura, M., and Elowitz, M.B. (2016). Dynamics of epigenetic regulation at the single-cell level. Science *351*, 720-724.

Blythe, S.A., and Wieschaus, E.F. (2016). Establishment and maintenance of heritable chromatin structure during early Drosophila embryogenesis. Elife *5*, e20148.

Bothma, J.P., Garcia, H.G., Ng, S., Perry, M.W., Gregor, T., and Levine, M. (2015). Enhancer additivity and non-additivity are determined by enhancer strength in the Drosophila embryo. Elife *4*, e07956.

Carninci, P., Sandelin, A., Lenhard, B., Katayama, S., Shimokawa, K., Ponjavic, J., Semple, C.A., Taylor, M.S., Engstrom, P.G., Frith, M.C.*, et al.* (2006). Genome-wide analysis of mammalian promoter architecture and evolution. Nat. Genet. *38*, 626-635.

Chen, H., Levo, M., Barinov, L., Fujioka, M., Jaynes, J.B., and Gregor, T. (2018). Dynamic interplay between enhancer-promoter topology and gene activity. Nat. Genet. *50*, 1296-1303.

Choi, J., Lysakovskaia, K., Stik, G., Demel, C., Soding, J., Tian, T.V., Graf, T., and Cramer, P. (2021). Evidence for additive and synergistic action of mammalian enhancers during cell fate determination. Elife *10*, e65381.

Choubey, S., Kondev, J., and Sanchez, A. (2015). Deciphering Transcriptional Dynamics In Vivo by Counting Nascent RNA Molecules. PLoS Comput. Biol. *11*, e1004345.

Davuluri, R.V., Suzuki, Y., Sugano, S., Plass, C., and Huang, T.H. (2008). The functional consequences of alternative promoter use in mammalian genomes. Trends Genet. *24*, 167-177.

de Klerk, E., and t Hoen, P.A. (2015). Alternative mRNA transcription, processing, and translation: insights from RNA sequencing. Trends Genet. *31*, 128-139.

Doshi, J., Willis, K., Madurga, A., Stelzer, C., and Benenson, Y. (2020). Multiple Alternative Promoters and Alternative Splicing Enable Universal Transcription-Based Logic Computation in Mammalian Cells. Cell Rep *33*, 108437.

Driever, W., and Nusslein-Volhard, C. (1989). The bicoid protein is a positive regulator of hunchback transcription in the early Drosophila embryo. Nature *337*, 138-143.

Driever, W., Thoma, G., and Nusslein-Volhard, C. (1989). Determination of spatial domains of zygotic gene expression in the Drosophila embryo by the affinity of binding sites for the bicoid morphogen. Nature *340*,

363-367.

Eck, E., Liu, J., Kazemzadeh-Atoufi, M., Ghoreishi, S., Blythe, S.A., and Garcia, H.G. (2020). Quantitative dissection of transcription in development yields evidence for transcription-factor-driven chromatin accessibility. Elife *9*, e56429.

Elowitz, M.B., Levine, A.J., Siggia, E.D., and Swain, P.S. (2002). Stochastic gene expression in a single cell. Science *297*, 1183-1186.

Estrada, J., Wong, F., DePace, A., and Gunawardena, J. (2016). Information Integration and Energy Expenditure in Gene Regulation. Cell *166*, 234-244.

Femino, A.M., Fay, F.S., Fogarty, K., and Singer, R.H. (1998). Visualization of single RNA transcripts in situ. Science *280*, 585-590.

Ferraro, T., Lucas, T., Clemot, M., De Las Heras Chanes, J., Desponds, J., Coppey, M., Walczak, A.M., and Dostatni, N. (2016). New methods to image transcription in living fly embryos: the insights so far, and the prospects. Wiley Interdiscip Rev. Dev. Biol. *5*, 296-310.

Foo, S.M., Sun, Y., Lim, B., Ziukaite, R., O'Brien, K., Nien, C.Y., Kirov, N., Shvartsman, S.Y., and Rushlow, C.A. (2014). Zelda potentiates morphogen activity by increasing chromatin accessibility. Curr. Biol. *24*, 1341-1346.

Fukaya, T., Lim, B., and Levine, M. (2016). Enhancer Control of Transcriptional Bursting. Cell *166*, 358-368.

Furlong, E.E.M., and Levine, M. (2018). Developmental enhancers and chromosome topology. Science *361*, 1341-1345.

Garcia, H.G., Tikhonov, M., Lin, A., and Gregor, T. (2013). Quantitative imaging of transcription in living Drosophila embryos links polymerase activity to patterning. Curr. Biol. *23*, 2140-2145.

Ghavi-Helm, Y., Klein, F.A., Pakozdi, T., Ciglar, L., Noordermeer, D., Huber, W., and Furlong, E.E. (2014). Enhancer loops appear stable during development and are associated with paused polymerase. Nature *512*, 96-100.

Gregor, T., Tank, D.W., Wieschaus, E.F., and Bialek, W. (2007). Probing the limits to positional information. Cell *130*, 153-164.

Haberle, V., and Stark, A. (2018). Eukaryotic core promoters and the functional basis of transcription initiation. Nat. Rev. Mol. Cell Biol. *19*, 621-637.

He, F., Ren, J., Wang, W., and Ma, J. (2011). A multiscale investigation of bicoid-dependent transcriptional events in Drosophila embryos. PLoS One *6*, e19122.

Hnisz, D., Day, D.S., and Young, R.A. (2016). Insulated Neighborhoods: Structural and Functional Units of Mammalian Gene Control. Cell *167*, 1188-1200.

Hortsch, S.K., and Kremling, A. (2019). Stochastic Models for Studying the Role of Cellular Noise and Heterogeneity, Reference Module in Biomedical Sciences. 10.1016/B978-0-12-801238-3.11466-7.

Kvon, E.Z., Kazmar, T., Stampfel, G., Yanez-Cuna, J.O., Pagani, M., Schernhuber, K., Dickson, B.J., and Stark, A.

(2014). Genome-scale functional characterization of Drosophila developmental enhancers in vivo. Nature *512*, 91-95.

Kvon, E.Z., Waymack, R., Gad, M., and Wunderlich, Z. (2021). Enhancer redundancy in development and disease. Nat. Rev. Genet. *22*, 324-336.

Lammers, N.C., Galstyan, V., Reimer, A., Medin, S.A., Wiggins, C.H., and Garcia, H.G. (2020). Multimodal transcriptional control of pattern formation in embryonic development. Proc. Natl. Acad. Sci. U S A *117*, 836-847.

Landry, J.R., Mager, D.L., and Wilhelm, B.T. (2003). Complex controls: the role of alternative promoters in mammalian genomes. Trends Genet. *19*, 640-648.

Lehmann, R., and Nusslein-Volhard, C. (1987). hunchback, a gene required for segmentation of an anterior and posterior region of the Drosophila embryo. Dev. Biol. *119*, 402-417.

Lenstra, T.L., Rodriguez, J., Chen, H., and Larson, D.R. (2016). Transcription Dynamics in Living Cells. Annu. Rev. Biophys. *45*, 25-47.

Levine, M. (2010). Transcriptional enhancers in animal development and evolution. Curr. Biol. *20*, 754-763.

Li, J., Hsu, A., Hua, Y., Wang, G., Cheng, L., Ochiai, H., Yamamoto, T., and Pertsinidis, A. (2020). Single-gene imaging links genome topology, promoter-enhancer communication and transcription control. Nat. Struct. Mol. Biol. *27*, 1032-1040.

Li, J.R., Dong, A.K., Saydaminova, K., Chang, H., Wang, G.S., Ochiai, H., Yamamoto, T., and Pertsinidis, A. (2019). Single-Molecule Nanoscopy Elucidates RNA Polymerase II Transcription at Single Genes in Live Cells. Cell *178*, 491-506.

Li, X., Lin, Z., Wang, H., Zhao, D., Xu, X., Wei, Y., Li, X., Li, X., Xiang, Y., Terada, L.S.*, et al.* (2018). Heritable, Allele-Specific Chromosomal Looping between Tandem Promoters Specifies Promoter Usage of SHC1. Mol. Cell. Biol. *38*, e0065817.

Li, X.Y., Harrison, M.M., Villalta, J.E., Kaplan, T., and Eisen, M.B. (2014). Establishment of regions of genomic activity during the Drosophila maternal to zygotic transition. Elife *3*, e03737.

Lim, B., Heist, T., Levine, M., and Fukaya, T. (2018). Visualization of Transvection in Living Drosophila Embryos. Mol. Cell *70*, 287-296.

Ling, J., Umezawa, K.Y., Scott, T., and Small, S. (2019). Bicoid-Dependent Activation of the Target Gene hunchback Requires a Two-Motif Sequence Code in a Specific Basal Promoter. Mol. Cell *75*, 1178-1187.

Little, S.C., Tikhonov, M., and Gregor, T. (2013). Precise developmental gene expression arises from globally stochastic transcriptional activity. Cell *154*, 789-800.

Liu, J., and Ma, J. (2013). Dampened regulates the activating potency of Bicoid and the embryonic patterning outcome in Drosophila. Nat. Commun. *4*, 2968.

Lopes, F.J., Spirov, A.V., and Bisch, P.M. (2012). The role of Bicoid cooperative binding in the patterning of sharp borders in Drosophila melanogaster. Dev. Biol. *370*, 165-172.

Lopes, F.J., Vanario-Alonso, C.E., Bisch, P.M., and Vieira, F.M. (2005). A kinetic mechanism for Drosophila bicoid cooperative binding. J. Theor. Biol. *235*, 185-198.

Lu, D., Sin, H.S., Lu, C., and Fuller, M.T. (2020). Developmental regulation of cell type-specific transcription by novel promoter-proximal sequence elements. Genes Dev. *34*, 663-677.

Lucas, T., Ferraro, T., Roelens, B., De Las Heras Chanes, J., Walczak, A.M., Coppey, M., and Dostatni, N. (2013). Live imaging of bicoid-dependent transcription in Drosophila embryos. Curr. Biol. *23*, 2135-2139.

Ma, X., Yuan, D., Diepold, K., Scarborough, T., and Ma, J. (1996). The Drosophila morphogenetic protein Bicoid binds DNA cooperatively. Development *122*, 1195-1206.

Mahan, B.H. (1975). Microscopic reversibility and detailed balance. An analysis. J. Chem. Educ. *52*, 299.

Margolis, J.S., Borowsky, M.L., Steingrimsson, E., Shim, C.W., Lengyel, J.A., and Posakony, J.W. (1995). Posterior stripe expression of hunchback is driven from two promoters by a common enhancer element. Development *121*, 3067-3077.

Mukaka, M.M. (2012). Statistics corner: A guide to appropriate use of correlation coefficient in medical research. Malawi Med. J. *24*, 69-71.

Munsky, B., and Khammash, M. (2008). Transient analysis of stochastic switches and trajectories with applications to gene regulatory networks. IET. Syst. Biol. *2*, 323-333.

Munsky, B., Neuert, G., and van Oudenaarden, A. (2012). Using gene expression noise to understand gene regulation. Science *336*, 183-187.

Neuert, G., Munsky, B., Tan, R.Z., Teytelman, L., Khammash, M., and van Oudenaarden, A. (2013). Systematic identification of signal-activated stochastic gene regulation. Science *339*, 584-587.

Nien, C.Y., Liang, H.L., Butcher, S., Sun, Y., Fu, S., Gocha, T., Kirov, N., Manak, J.R., and Rushlow, C. (2011). Temporal coordination of gene networks by Zelda in the early Drosophila embryo. PLoS Genet. *7*, e1002339.

Oudelaar, A.M., Davies, J.O.J., Hanssen, L.L.P., Telenius, J.M., Schwessinger, R., Liu, Y., Brown, J.M., Downes, D.J., Chiariello, A.M., Bianco, S.*, et al.* (2018). Single-allele chromatin interactions identify regulatory hubs in dynamic compartmentalized domains. Nat. Genet. *50*, 1744-1751.

Ozbudak, E.M., Thattai, M., Kurtser, I., Grossman, A.D., and van Oudenaarden, A. (2002). Regulation of noise in the expression of a single gene. Nat. Genet. *31*, 69-73.

Pare, A., Lemons, D., Kosman, D., Beaver, W., Freund, Y., and McGinnis, W. (2009). Visualization of individual Scr mRNAs during Drosophila embryogenesis yields evidence for transcriptional bursting. Curr. Biol. *19*, 2037-2042.

Peccoud, J., and Ycart, B. (1995). Markovian Modeling of Gene-Product Synthesis. Theor. Popul. Biol. *48*, 222-

234.

Perry, M.W., Boettiger, A.N., and Levine, M. (2011). Multiple enhancers ensure precision of gap gene-expression patterns in the Drosophila embryo. Proc. Natl. Acad. Sci. U S A *108*, 13570-13575.

Perry, M.W., Bothma, J.P., Luu, R.D., and Levine, M. (2012). Precision of hunchback expression in the Drosophila embryo. Curr. Biol. *22*, 2247-2252.

Petrascheck, M., Escher, D., Mahmoudi, T., Verrijzer, C.P., Schaffner, W., and Barberis, A. (2005). DNA looping induced by a transcriptional enhancer in vivo. Nucleic Acids Res. *33*, 3743-3750.

Phillips-Cremins, J.E., and Corces, V.G. (2013). Chromatin insulators: linking genome organization to cellular function. Mol. Cell *50*, 461-474.

Porcher, A., Abu-Arish, A., Huart, S., Roelens, B., Fradin, C., and Dostatni, N. (2010). The time to measure positional information: maternal hunchback is required for the synchrony of the Bicoid transcriptional response at the onset of zygotic transcription. Development *137*, 2795-2804.

Pozner, A., Lotem, J., Xiao, C., Goldenberg, D., Brenner, O., Negreanu, V., Levanon, D., and Groner, Y. (2007). Developmentally regulated promoter-switch transcriptionally controls Runx1 function during embryonic hematopoiesis. BMC Dev. Biol. *7*, 84.

Rach, E.A., Yuan, H.Y., Majoros, W.H., Tomancak, P., and Ohler, U. (2009). Motif composition, conservation and condition-specificity of single and alternative transcription start sites in the Drosophila genome. Genome Biol. *10*, R73.

Raj, A., Peskin, C.S., Tranchina, D., Vargas, D.Y., and Tyagi, S. (2006). Stochastic mRNA synthesis in mammalian cells. PLoS Biol. *4*, e309.

Raj, A., van den Bogaard, P., Rifkin, S.A., van Oudenaarden, A., and Tyagi, S. (2008). Imaging individual mRNA molecules using multiple singly labeled probes. Nat. Methods *5*, 877-879.

Rieckh, G., and Tkacik, G. (2014). Noise and information transmission in promoters with multiple internal States. Biophys. J. *106*, 1194-1204.

Rosenfeld, N., Young, J.W., Alon, U., Swain, P.S., and Elowitz, M.B. (2005). Gene regulation at the single-cell level. Science *307*, 1962-1965.

Sanchez, A., and Golding, I. (2013). Genetic determinants and cellular constraints in noisy gene expression. Science *342*, 1188-1193.

Schmidt, U., Basyuk, E., Robert, M.C., Yoshida, M., Villemin, J.P., Auboeuf, D., Aitken, S., and Bertrand, E. (2011). Real-time imaging of cotranscriptional splicing reveals a kinetic model that reduces noise: implications for alternative splicing regulation. J. Cell Biol. *193*, 819-829.

Scholes, C., Biette, K.M., Harden, T.T., and DePace, A.H. (2019). Signal Integration by Shadow Enhancers and Enhancer Duplications Varies across the Drosophila Embryo. Cell Rep *26*, 2407-2418.

Schroder, C., Tautz, D., Seifert, E., and Jackle, H. (1988). Differential regulation of the two transcripts from the Drosophila gap segmentation gene hunchback. EMBO J. *7*, 2881-2887.

Schulz, K.N., Bondra, E.R., Moshe, A., Villalta, J.E., Lieb, J.D., Kaplan, T., McKay, D.J., and Harrison, M.M. (2015). Zelda is differentially required for chromatin accessibility, transcription factor binding, and gene expression in the early Drosophila embryo. Genome Res. *25*, 1715-1726.

Sendoel, A., Dunn, J.G., Rodriguez, E.H., Naik, S., Gomez, N.C., Hurwitz, B., Levorse, J., Dill, B.D., Schramek, D., Molina, H.*, et al.* (2017). Translation from unconventional 5' start sites drives tumour initiation. Nature *541*, 494-499.

Senecal, A., Munsky, B., Proux, F., Ly, N., Braye, F.E., Zimmer, C., Mueller, F., and Darzacq, X. (2014). Transcription factors modulate c-Fos transcriptional bursts. Cell Rep. *8*, 75-83.

Singh, J., and Padgett, R.A. (2009). Rates of in situ transcription and splicing in large human genes. Nat. Struct. Mol. Biol. *16*, 1128-1133.

Skinner, S.O., Sepulveda, L.A., Xu, H., and Golding, I. (2013). Measuring mRNA copy number in individual Escherichia coli cells using single-molecule fluorescent in situ hybridization. Nat. Protoc. *8*, 1100-1113.

Spitz, F., and Furlong, E.E. (2012). Transcription factors: from enhancer binding to developmental control. Nat. Rev. Genet. *13*, 613-626.

Struhl, G., Struhl, K., and Macdonald, P.M. (1989). The gradient morphogen bicoid is a concentration-dependent transcriptional activator. Cell *57*, 1259-1273.

Su, W., Jackson, S., Tjian, R., and Echols, H. (1991). DNA looping between sites for transcriptional activation: self-association of DNA-bound Sp1. Genes Dev. *5*, 820-826.

Sun, Y., Nien, C.Y., Chen, K., Liu, H.Y., Johnston, J., Zeitlinger, J., and Rushlow, C. (2015). Zelda overcomes the high intrinsic nucleosome barrier at enhancers during Drosophila zygotic genome activation. Genome Res. *25*, 1703-1714.

Swinstead, E.E., Miranda, T.B., Paakinaho, V., Baek, S., Goldstein, I., Hawkins, M., Karpova, T.S., Ball, D., Mazza, D., Lavis, L.D.*, et al.* (2016). Steroid Receptors Reprogram FoxA1 Occupancy through Dynamic Chromatin Transitions. Cell *165*, 593-605.

Tautz, D., Lehmann, R., Schnurch, H., Schuh, R., Seifert, E., Kienlin, A., Jones, K., and Jackle, H. (1987). Finger protein of novel structure encoded by hunchback, a second member of the gap class of Drosophila segmentation genes. Nature *327*, 383-389.

Ushijima, T., Hanada, K., Gotoh, E., Yamori, W., Kodama, Y., Tanaka, H., Kusano, M., Fukushima, A., Tokizawa, M., Yamamoto, Y.Y.*, et al.* (2017). Light Controls Protein Localization through Phytochrome-Mediated Alternative Promoter Selection. Cell *171*, 1316-1325.

Vernimmen, D., and Bickmore, W.A. (2015). The Hierarchy of Transcriptional Activation: From Enhancer to Promoter. Trends Genet. *31*, 696-708.

Voss, T.C., and Hager, G.L. (2014). Dynamic regulation of transcriptional states by chromatin and transcription factors. Nat Rev Genet *15*, 69-81.

Waymack, R., Fletcher, A., Enciso, G., and Wunderlich, Z. (2020). Shadow enhancers can suppress input transcription factor noise through distinct regulatory logic. Elife *9*, e59351.

Wu, X., Vasisht, V., Kosman, D., Reinitz, J., and Small, S. (2001). Thoracic patterning by the Drosophila gap gene hunchback. Dev. Biol. *237*, 79-92.

Xu, H., Sepúlveda, L.A., Figard, L., Sokac, A.M., and Golding, I. (2015). Combining protein and mRNA quantification to decipher transcriptional regulation. Nat. Methods *12*, 739–742.

Xu, H., Skinner, S.O., Sokac, A.M., and Golding, I. (2016). Stochastic Kinetics of Nascent RNA. Phys. Rev. Lett. *117*, 128101.

Zenklusen, D., Larson, D.R., and Singer, R.H. (2008). Single-RNA counting reveals alternative modes of gene expression in yeast. Nat. Struct. Mol. Biol. *15*, 1263-1271.

Zoller, B., Little, S.C., and Gregor, T. (2018). Diverse Spatial Expression Patterns Emerge from Unified Kinetics of Transcriptional Bursting. Cell *175*, 835-847.

Figure 1

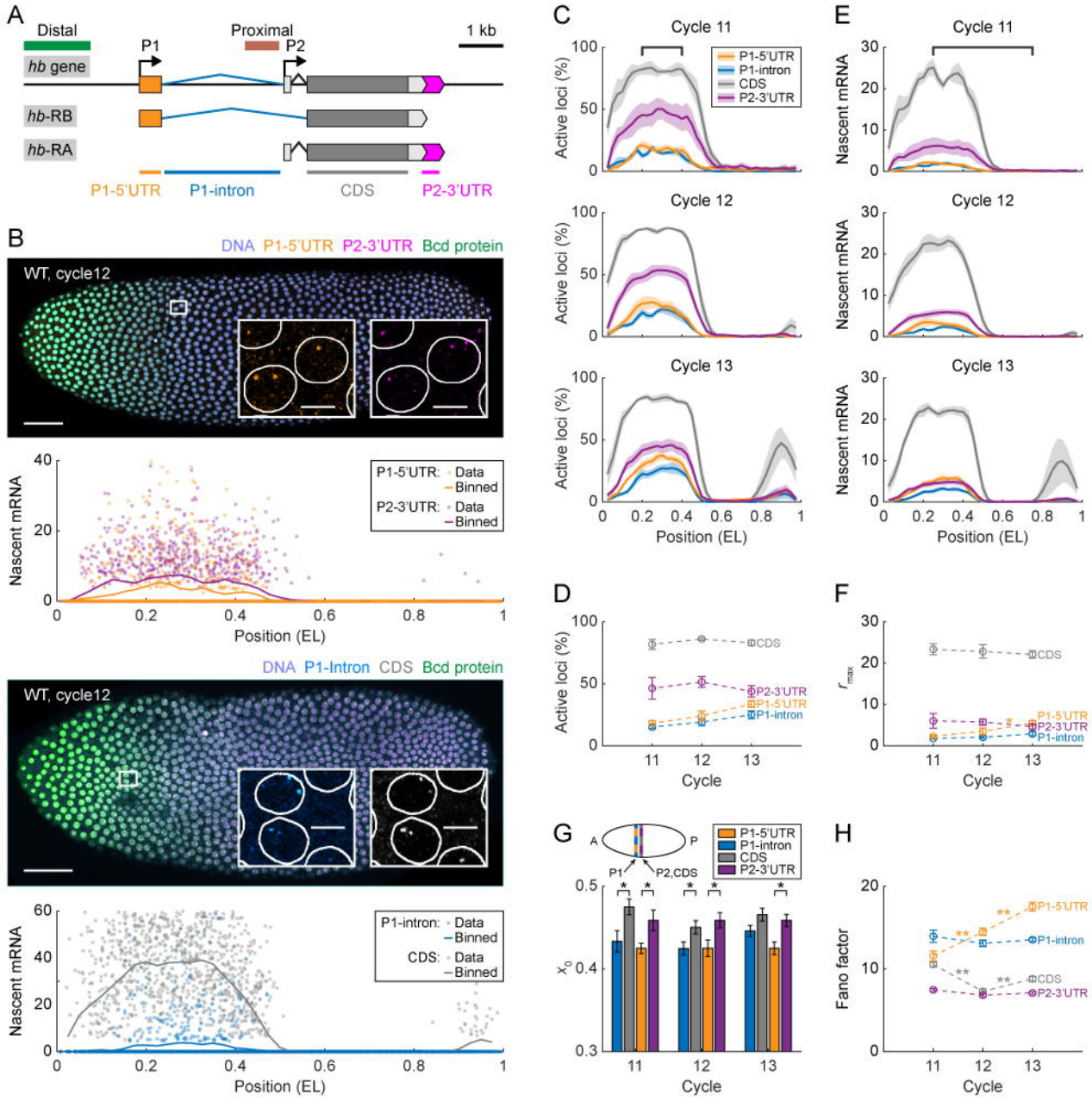

Figure 2

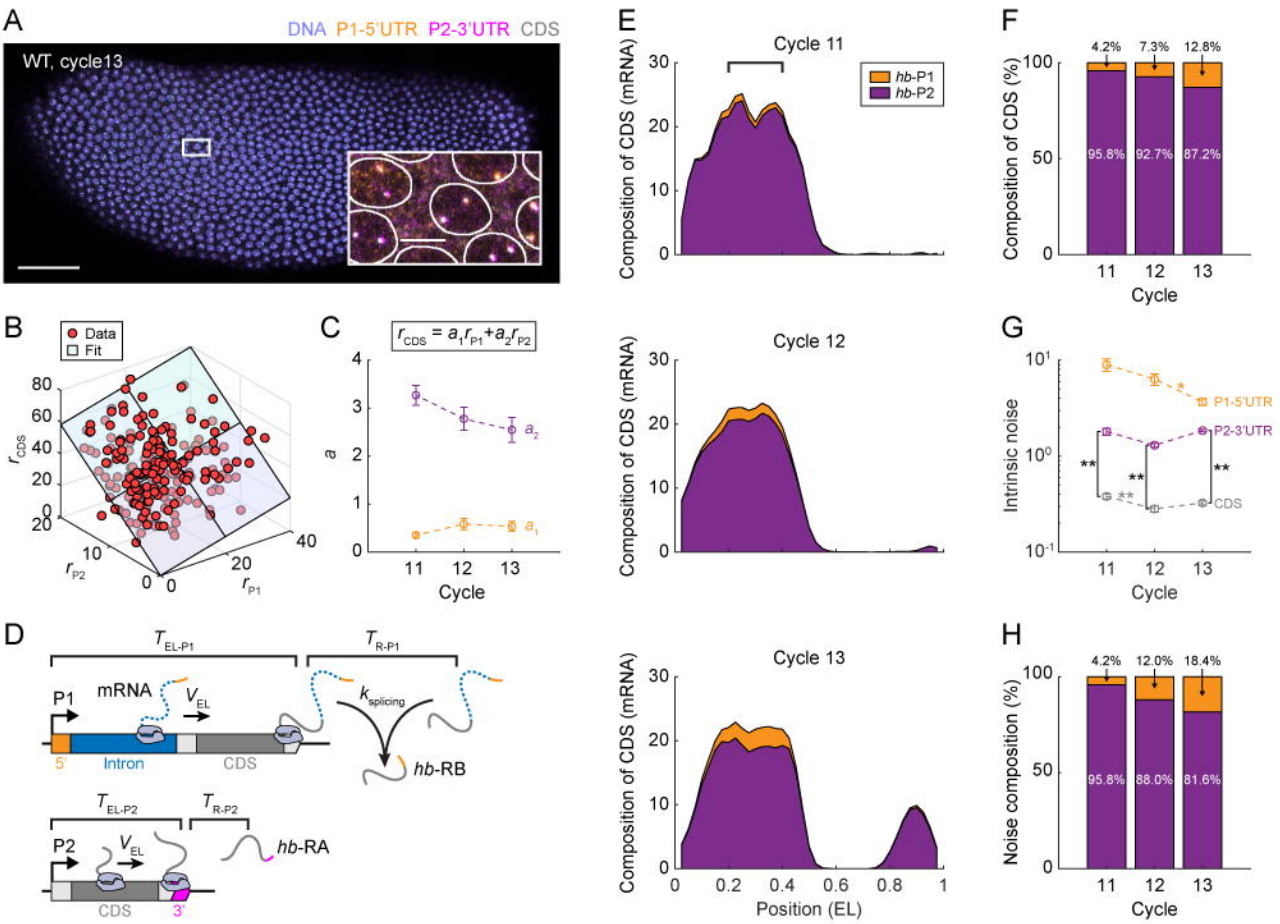

Figure 3

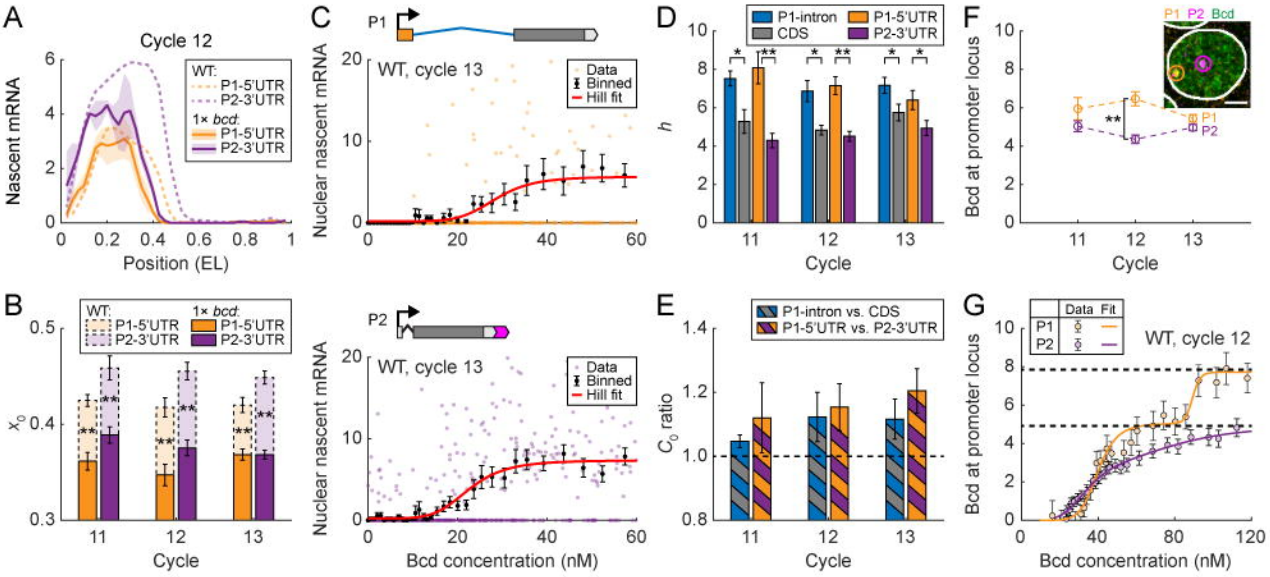

Figure 4

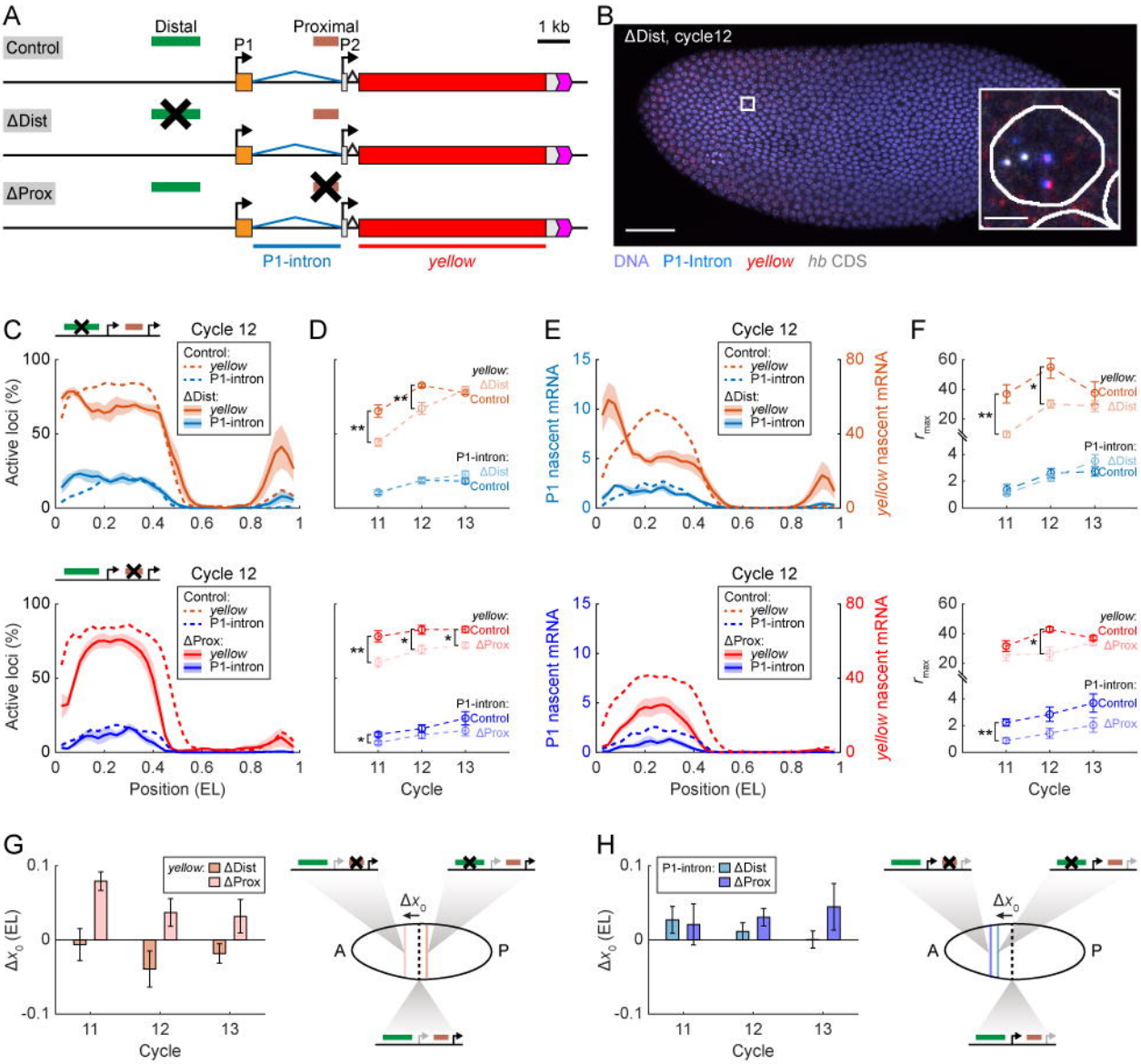

Figure 5